ISSN1346-7832

独立行政法人港湾空港技術研究所

港湾空港技術研究所報告

REPORT OF THE PORT AND AIRPORT RESEARCH INSTITUTE

VOL.42 NO.2 June 2003

NAGASE,YOKOSUKA,JAPAN
INDEPENDENT ADMINISTRATIVE INSTITUTION,
PORT AND AIRPORT RESEARCH INSTITUTE

港湾空港技術研究所報告（REPORT OF PARI）
第42巻　第2号（Vol. 42, No. 2），2003年6月（June 2003）

目　　次（CONTENTS）

TECHNICAL REPORT OF THE PORT AND
AIRPORT RESEARCH INSTITUTE
Vol. 42, No. 2, June 2003.

Long-term Durability of Concrete Made with Slag Cements Under Marine Environment

Tarek Uddin MOHAMMED*

Hidenori HAMADA**

Toru YAMAJI***

Synopsis

Marine structures show earlier deterioration mainly due to the corrosion of steel bars in concrete caused by the chloride ingress from seawater. Prevention of chloride ingress is a great hurdle to make long-term durable concrete structures. Based on the investigations on the short-term accelerated laboratory and natural exposure, it was understood that utilization of slag cement results in significant reduction in chloride ingress compared to the commonly used ordinary portland cement (OPC). To verify it's long-term performance, three series of specimens were exposed to the marine exposure zone of *Port and Airport Research Institute*, a very special and rare exposure facility in the world. Recently the age of the specimens became 10, 15, and 30 years for these series. Physical appearance, compressive strength, carbonation depth, evaporable water content, concrete resistance, water and acid soluble chloride ingress, microstructures, mineralogy, corrosion of steel bars in concrete, and interfaces of concrete were evaluated and compared with OPC. All of these results are summarized here. The results will be very useful to the concrete professionals dealing with the long-term durability of marine concrete structures.

No harmful effect of using slag cements is found after long-term exposure. Compared to OPC, slag cement shows more long-term strength gain. The outer crust of the specimens made with slag cements becomes denser after a long-term of exposure. It screens chloride at the outer crust of the specimens. Corrosion of steel bars in concrete is very low for slag cement. Relatively denser interface and microstructure are found for concrete made with slag cements. It is clearly understood that slag cement can be used for making long-term durable concrete structures. Besides the above-mentioned results, it is also found that voids at the steel-concrete interface initiate corrosion even for a low chloride concentration. Improvement of the steel-concrete interface is necessary to ensure long-term durability of marine concrete structures.

Key Words: compressive strength, corrosion, durability, marine environment, interfaces, microstructures, mineralogy, slag cements.

* Research Engineer (Senior), Materials Division, Geotechnical and Structural Engineering Department
** Chief Research Engineer, Materials Division, Geotechnical and Structural Engineering Department
*** Research Engineer, Materials Division, Geotechnical and Structural Engineering Department
3-1-1 Nagase, Yokosuka, 239-0826 Japan.
Phone : +81-468-44-5061 Fax : +81-468-44-0255 e-mail : tarek@pari.go.jp

港湾空港技術研究所報告
第42巻第2号(2003.6)

スラグセメントを用いたコンクリートの海洋環境下における長期耐久性

タレク　ウディン　モハメッド*・濵田　秀則**・山路　徹***

要　旨

多くの海洋コンクリート構造物において，海水中の塩化物イオンがもとで生じる鉄筋腐食による早期劣化が発生している．塩化物イオンの浸透をどのように抑制するかは，構造物の長期耐久性を実現するための重要な課題である．各種の比較的短期間の実環境暴露試験や促進試験の結果から，スラグセメントを使用したコンクリートにおいては普通ポルトランドセメントを使用したコンクリートに比べて塩化物イオンの浸透が抑制されていることが明らかになっている．この抑制効果の長期的挙動を把握するために，3種の異なるシリーズの，スラグセメントを用いたコンクリートの長期暴露試験を港空研構内の海水循環水槽において実施した．これらのシリーズの暴露期間が各々30年，15年，10年に達したことから，供試体の評価試験を実施した．コンクリートの外観性状，圧縮強度，中性化深さ，含水率，コンクリートの電気抵抗，塩化物イオン含有量（全塩化物・可溶性塩化物），細孔構造，鉱物組成，埋設鉄筋の腐食状況，鉄筋－コンクリート界面の観察，を実施し，普通ポルトランドセメントコンクリートとの比較を行った．これらの一連の実験の結果を本文では取りまとめる．本文において述べられている結果は，海洋環境下におけるコンクリートの長期耐久性を考察する上で貴重な資料となるものである．

長期間の暴露を経た供試体の試験結果では，スラグセメントを使用することによるマイナス面の効果は皆無であった．普通ポルトランドセメントを使用したコンクリートに比べて，スラグセメントコンクリートの方が長期的な強度の増進を示した．スラグセメントコンクリートの供試体の表層部は，長期間の暴露後に密実になる傾向を示し，それにより塩化物イオンが表層部で遮へいされていた．また，内部鉄筋の腐食もスラグセメントコンクリートの方が軽微であった．また，スラグセメントの方が緻密な細孔構造を示すと同時に，鉄筋－コンクリート界面構造も緻密であった．これより，スラグセメントコンクリートの方が長期耐久性に優れるものと判断された．

また，上記の結果に加え，鉄筋－コンクリート界面に空隙が存在すると塩化物イオン濃度がかなり低くても鉄筋の腐食が開始されることから，海洋コンクリート構造物の長期耐久性を向上させるためには，鉄筋－コンクリート界面の構造を改善することが極めて重要であることが明らかとなった．

キーワード：圧縮強度，腐食，耐久性，海洋環境，界面，細孔構造，鉱物組成，スラグセメント

*　地盤・構造部　材料研究室　研究官（シニア）
**　地盤・構造部　材料研究室　室長
***　地盤・構造部　構造強度研究室　研究官
〒239－0826　神奈川県横須賀市長瀬3－1－1　独立行政法人港湾空港技術研究所
TEL：0468－44－5061　FAX：0468－44－0255　e－mail：tarek@pari.go.jp

Contents

1. Introduction

Concrete, a commonly used construction materials, is accepted all over the world since long ago. Concrete consumption in the year of 2000 is estimated at 12 billion tons (**1**). Based on the estimated world population in the year of 2000 at six billion, it can also be simply estimated that two tons of concrete is placed per capita per year. Due to the rapid development of the infrastructures of the developing countries, it is expected that in the year of 2050, the annual consumption of concrete will reach 18 billion tons per year. To produce this concrete, 2.3 billion tons of cement will be necessary. As one ton of carbon dioxide is emitted to the atmosphere per ton of cement production, therefore it can be realized that 2.3 billion tons of CO_2 will be added to the greenhouse gases from the cement production (about 7% of total green house gases produce globally). Also, in making this large amount of concrete, a huge amount of energy will be necessary to produce cement, aggregate, mixing, placing of concrete. Also, a significant amount of natural resources (for making aggregates and cements) will have to be demolished for the production of this huge volume of concrete. Therefore, it is clearly realized that making long-term durable concrete is very important to reduce the rate of these negative influences to the environment.

In the marine environment, concrete structures deteriorate earlier mainly due to the corrosion of steel bars in concrete caused by the chlorides ingress from seawater. Prevention of the chloride ingress is a simple process for the long-term durability. Fortunately, it was found that slag cement reduces chloride ingress in concrete significantly. Steel making industries are also facing a severe problem to dispose this by-product. Therefore, utilization of this by-product will give several great benefits, such as saving the cements, and solving the disposal problem, making long-term durable concrete, and reduction of CO_2 emission. The generated $Ca(OH)_2$ in the hydration process of portland cement reacts with the slag particles and improve the microstructure. It reduces the capillary pore volume of concrete. This process is well understood based on the short-term laboratory and natural exposures. However, long-term performance of concrete made with slag cements is still necessary to confirm it's acceptability whole over the world.

With this background, three different series of specimens were made before 10, 15, and 30 years. The specimens were exposed to the very special and rare marine exposure facility of *Port and Airport Research Institute* using seawater directly taken from the sea. Physical appearance, compressive strength, carbonation depth, evaporable water content in concrete, concrete resistance, water and acid soluble chloride ingress, microstructures, mineralogy, corrosion of steel bars in concrete, and interfaces of concrete were evaluated and compared with OPC. All of these results are summarized here and will be very useful to make decision for making long-term durable marine concrete structures. Results of these investigations are also reported in **References 2~7.**

2. Experimentation

2.1 Scope

Three series (Series 1, 2, 3) of the specimens made with slag cements were investigated at the exposure age of 10 (for Series 1), 15 (for Series 2), and 30 (for Series 3) years. In Series 1, the variables include ordinary portland cement (OPC), slag cement, slag fineness (Blaine fineness 4000 and 8000 cm^2/g), slag replacement amount (40, 55, 70%), and exposure zone (tidal and splash). In Series 2, the variables include OPC, different kinds of slag cements (Type A, B, and C), exposure zone (tidal and submerged). In Series 3, the variables include OPC and slag cement. In Series 2, both uncracked and pre-cracked specimens were investigated. In other series, only the uncracked specimens were investigated. Others variables, such as mixing water as tap water and seawater, sulfate content, fly ash cement, different water reducing chemical admixtures (naphthalene, melamine, polycarboxyl, amino sulfonate, vinsol), shrinkage reducing admixtures, and other cements, such as high early strength cement, moderate heat cement, and alumina cement were also investigated, however, they are not covered here. Results on these variables can be obtained from **References 2~7.** The specimens were tested for physical appearance, compressive strength, carbonation depth, evaporable water content in concrete, concrete resistance, water and acid soluble chloride ingress, microstructures, mineralogy, corrosion of steel bars and interfaces of concrete.

Table 1 Aggregate Properties – Series 1

	Specific Gravity	Absorption (%)	Fineness Modulus
Sand	2.63	1.63	2.73
Gravel	2.64	0.6	6.64

Table 2 Physical and Chemical Compositions of Cement and Slags – Series 1

	OPC	Slag 1	Slag 2
Specific Gravity	3.16	2.90	2.90
Blaine Fineness, cm^2/g	3190	7900	4080
Loss of Ignition, %	0.7	-	-
SiO_2, %	21.3	32.7	33.2
Al_2O_3, %	5.3	13.8	14.1
CaO, %	64.4	42.4	42.3
MgO, %	2.2	5.9	5.9
SO_3, %	1.9	2.0	2.0
Na_2O, %	0.28	-	-
K_2O, %	0.6	-	-
Fe_2O_3, %	2.6	0.2	0.2

\- Indicate not measured items

Table 3 Chemical Compositions of Steel Bar–Series 1~3

C (%)	Si (%)	Mn (%)	P (%)	S (%)
0.1	0.21	0.66	0.02	0.02

Table 4 Aggregate Properties – Series 2

	Specific Gravity	Absorption (%)	Fineness Modulus
Sand	2.64	1.82	2.89
Gravel	2.76	1.10	6.66

Table 5 Physical and Chemical Compositions of Cements - Series 2

Items	SCA	SCB	SCC
Specific Gravity	3.07	3.03	2.97
Blaine Fineness, cm^2/g	3610	3700	3980
Ignition Loss, %	0.9	0.7	0.9
SiO_2, %	24.9	26.5	28.9
Al_2O_3, %	7.8	9.2	11.3
CaO, %	56.8	53.4	47.9
MgO, %	3.8	4.3	5.2
SO_3, %	2.0	2.0	2.0
Fe_2O_3, %	2.0	1.8	1.1

OPC satisfied JIS R5210; SCA, SCB and SCC satisfied JIS R5211.

Table 6 Classifications of Slag Cements (JIS R5211-1992)

Type	Slag Content (Mass %)
Slag Cement A	5~30
Slag Cement B	30~60
Slag Cement C	60~70

Table 7 Physical and Chemical Compositions of Cements – Series 3

	OPC	SCB
Specific Gravity	3.14	3.04
Blaine Fineness (cm2/g)	3180	3850
Ignition Loss, %	0.8	0.4
SiO_2, %	21.7	25.7
Al_2O_3, %	5.5	9.7
CaO, %	64.7	54.1
MgO, %	1.3	3.2
SO_3, %	2.0	2.4
Fe_2O_3, %	3.1	2.1
Na2O,%	0.3	0.46
K2O	0.57	0.51

- Not Available

Table 8 Mixture Proportion of Concrete - Series 1

	OPC	SC-55	SF-55	SF-40	SF-70
G_{max} (mm)	20	20	20	20	20
Slump (cm)	12±1	12±1	12±1	12±1	12±1
Air (%)	4±1	4±1	4±1	4±1	4±1
W/C (%)	47.0	47.0	47.0	47.0	47.0
S/a (%)	46	45.5	45.3	45.5	45.4
W (kg/m^3)	155	155	155	155	155
C (kg/m^3)	330	330	330	330	330
S (kg/m^3)	847	831	828	834	828
G (kg/m^3)	1001	1001	1001	1001	1001
HRWRAEA (% of C)	1.5	1.5	1.5	1.5	1.5
AEA (mL/m^3)	0.0015	0.005	0.006	0.005	0.0095

W, C, G, and S mean water, cement, gravel and sand. s/a is sand-aggregate ratio. HRWRAEA means high-range water-reducing and air-entraining admixture (naphthalene based). AEA means air-entraining admixture.

Table 9 Mixture Proportions of Concrete – Series 2

	OPC	SCA	SCB	SCC
G_{max} (mm)	20	20	20	20
Slump (cm)	8±1	8±1	8±1	8±1
Air (%)	4±1	4±1	4±1	4±1
W/C (%)	45	45	45	45
S/a (%)	41	42	41	41
W (kg/m^3)	162	160	160	162
C (kg/m^3)	360	356	355	360
S (kg/m^3)	738	756	736	714
G (kg/m^3)	1110	1091	1108	1120
AEWRA (kg/m^3)	3.60	3.56	3.55	3.60
AEA (mL/m^3)	360	356	355	360

Table 10 Mixture Proportions of Concrete – Series 3

	OPC	SCB
G_{max} (mm)	25	25
Slump (cm)	6.6	3.5
Air (%)	3.4	3.0
W/C (%)	52.7	52.4
s/a (%)	37	37
W (kg/m^3)	153	152
C (kg/m^3)	290	290
S (kg/m^3)	740	738
G (kg/m^3)	1261	1258
AEWRA (kg/m^3)	2.9	2.9
AEA (mL/m^3)	-	-

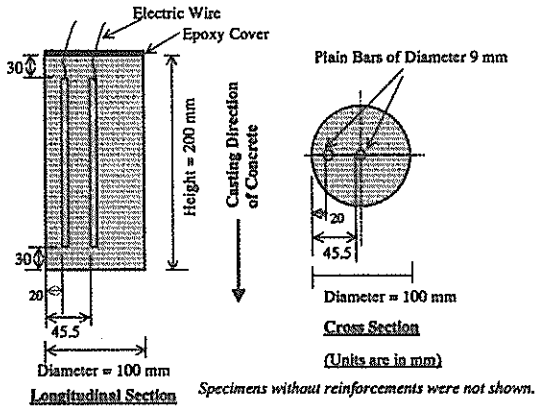

Fig. 1 Layout of the Specimens – Series 1

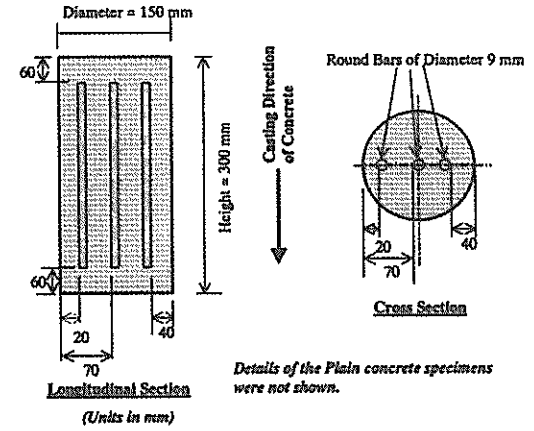

Fig. 2 Layout of the Specimens – Series 2 and 3

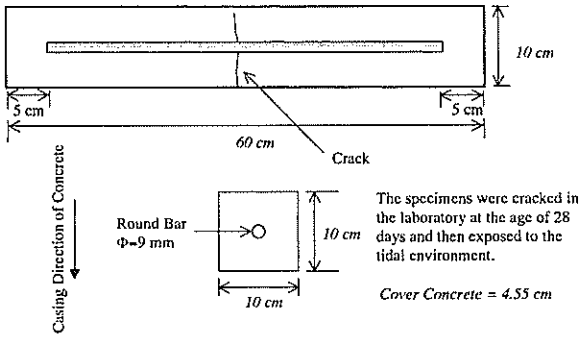

Fig. 3 Layout of the Specimens – Series 2 (Cracked)

2.2 Materials

River sand and crushed granite coarse aggregate were used in all series. Aggregate properties of Series 1 are shown in **Table 1**. The chemical composition of OPC and slags of Series 1 are summarized in **Table 2**. The chemical composition of steel bar is given in **Table 3**. It was same for all series. Aggregate properties and chemical composition of different slag cements of Series 2 are summarized in **Table 4**, and **5**, respectively. Classification of the different slag cements based on the slag content is summarized in **Table 6**. River gravel and river sand produced from Sagami River, Kanagawa, Japan were used in Series 3. Chemical compositions of cements of Series 3 are summarized in **Table 7**.

2.3 Mixture Proportions

Mixture proportion of concrete used in Series 1 (S1) is given in **Table 8**. SC-55 means coarse slag (Blaine fineness 4000 cm^2/g) with 55% replacement. SF-40, SF-55, and SF-70 mean fine slag (8000 cm^2/g) with 40, 55, and 70% replacement, respectively. The mixture proportions of Series 2 (S2) are summarized in **Table 9**. Here, the SCA, SCB, and SCC indicate the slag cements of Type A, B, and C, respectively. The slag contents of these cements are given in **Table 6**. The mixture proportions of Series 3 (S3) are given in **Table 10**. SCB means the slag cement of Type B as in Series 2.

2.4 Layout of the Specimens

In Series 1, plain and reinforced cylinder specimens of diameter 100 mm and length 200 mm were investigated as shown in **Fig. 1**. Two round (smooth) steel bars of diameter 9 mm and length 140 mm were embedded at cover depths of 20 and 45.5 mm. In Series 2 and 3, plain and reinforced cylinder specimens of diameter 150 mm and height 300 mm were made as shown in **Fig. 2**. Three round steel bars of diameter 9 mm and length 180 mm were embedded at cover depths of 20, 40 and 70 mm. In Series 2, in addition to the cylinder specimens, pre-cracked prism specimens were also investigated. The layout of the specimen is shown in **Fig. 3**. The size of the specimens was 10×10×60 cm. In each specimen, a round steel bar of diameter 9 mm and length 50 cm were embedded at a cover depth of 4.55 cm i.e., at the center of the specimen. After 28 days of standard curing, the specimens were cracked in the laboratory with a specified crack width and then exposed to the tidal zone (about 1 m below the high water level) of a tidal pool.

Table 11 Physical Properties and Chemical Composition of Seawater

Specific Gravity	pH	Na ppm	K ppm	Ca ppm	Mg ppm	Cl ppm	SO_4 ppm	CO_3 ppm
1.022	7.77	9290	346	356	1167	17087	2378	110

Table 12 Wetting and Drying Hours in the Tidal and Splash Exposure

Series	Tidal	Submerged	Splash
1	Wetting 4 hours and drying 8 hours	-	Spray 4 hours and air dry 8 hours.
2	Wetting 4.5 hours and drying 7.5 hours	Always Under Seawater	-
3	Wetting 5 hours and drying 7 hours	Always Under Seawater	-

- No specimen.

2.5 Exposure Conditions

After 28 days of standard curing, three plain concrete specimens were tested for compressive strength and Young's modulus of elasticity of concrete. Remaining specimens were exposed in a tidal pool or splash zone exposure located beside the sea at latitude of about 35° N and longitude of about 138° E. Natural seawater was automatically pumped into and drained out at six-hour interval in the tidal pool. The specimens were free from freezing and thawing effect. The compositions of seawater are given in **Table 11**. In the splash zone, one cycle consists of four hours spraying of seawater over the specimens and eight hours of air-drying under the open sky.

The tidal cycles and the splash exposure conditions are summarized in **Table 12**. The tidal cycles are estimated based on the location of the specimens in the tidal pool.

2.6 Method of Evaluations

At the age of 28-days, plain concrete specimens were tested for compressive strength and Young's modulus of elasticity of concrete as per JIS A1108 and JSCE G502, respectively. Also, after continuous exposure for 10 years (Tidal) for Series 1, and 15 years for Series 2 (Tidal), the specimens were tested for compressive strength.

For electro-chemical evaluation of corrosion, a portion (5 cm for Series 1, and 7 cm for Series 2 and 3) of the specimens was cut from the top by a diamond saw and the electric wires were connected with the steel bars. Then the cut surfaces were covered with an epoxy compound. Polarization resistance, concrete resistance, and half-cell potential (versus Ag/AgCl) were measured by a portable corrosion monitor. The polarization resistance and concrete resistance were measured by AC impedence method. For this, the high and low frequencies were set at 10 Hz and 10 mHz, respectively. Utilizing polarization resistance data, micro-cell current density of the steel bars was evaluated using the Stern-Geary equation given below (**8**):

$$I_{mic} = \frac{B}{R_p} \times 10^6 \quad (1)$$

$$B = \frac{\beta_a \beta_c}{2.3(\beta_a + \beta_c)} \quad (2)$$

Where, I_{mic} is the micro-cell current density over the steel bar in $\mu A / cm^2$, the value of B depends on the slopes of the anodic (β_a) and cathodic (β_c) polarization curves. Assuming, β_a and β_c as 120 mV/decade, the value of B can be estimated at 0.026 V (**8**). R_p is the polarization resistance in $\Omega.cm^2$.

After the above-mentioned electrochemical measurements, the anodic polarization curves of the steel bars were measured. For this, the potential of the steel bars was shifted from its natural potential to the positive value of 1 V with a scan speed of 1 mV/sec by a potentiostat. The passivity grades of the steel bars were evaluated from the measured anodic polarization curves (**9**). A higher grade of passivity represents a better degree of passivity. After all investigations, the specimens were broken open and the steel bars were collected.

The limiting cathodic current density over the steel bars was measured for some steel bars. It is necessary to mention that these steel bars were not tested for anodic polarization curves in order to avoid the effect of positive polarization. The limiting cathodic current density can be transferred to the oxygen permeability by using the following equation (**10**) :

$$\frac{dQ}{dt} = -\frac{I_{\lim}}{nF} \quad (3)$$

Where, $\frac{dQ}{dt}$ is the oxygen permeability in mole/cm^2/sec (on steel surface), I_{lim} is the limiting cathodic current density in A/cm^2, F is the Faraday's constant (96500 coulombs/mole) and n is 4. The limiting cathodic current density was measured by a potentiostat. The potential difference between the titanium mesh anode and steel element was kept at 860 mV.

Water and acid soluble chloride concentrations were measured at different depths from the surface. For this, a disc of 50 mm thick was cut from the mid-height of the plain concrete specimens. After that a 3 cm thick slice was cut from the center of the disk. It was cut again to take samples from the specified depths. The samples were powdered by a vibrating mill. Water and acid soluble chloride concentrations were measured as per JCI SC4. The following equation is commonly used to predict the apparent diffusion coefficient of chlorides in concrete (**11**):

$$C(x,t) = C_o\left(1 - erf\left[\frac{x}{2\sqrt{D_{ac}t}}\right]\right) \quad (4)$$

Where, $C(x,t)$ is the chloride concentration at a depth x (mm) and time t (year), C_o is the chloride concentration at the surface (here it is assumed to be equal to the chloride concentration at a mean sampling depth of 10 mm) as mass percentage of cement, D_{ac} is the apparent diffusion co-efficient in mm^2/year and *erf* is the error function. After evaluating the diffusion co-efficient, the time to initiate corrosion was measured considering the chloride threshold value at 0.4% of cement mass (**12**).

Carbonation depth of the specimens was evaluated after spraying 1% phenolphthalein solution on freshly cut or broken surfaces.

Porosity of the mortar samples was measured at the different depths (5-15 mm, 35-45 mm and 65-75 mm) of the specimens. For this, mortar pieces (approximate sizes 5 mm) were collected from the required depth and dried. Then pore size distribution of the samples was evaluated by mercury intrusion porosimeter.

The mineralogy of the powdered concrete samples at depths 5-15, 35-45, and 65-75 mm was evaluated by X-ray diffraction (XRD) method. For this, mortar portions were collected from the specified depths of the specimens. The samples were crushed and pulverized to an average particle size of less than 10 microns. Then a diffractometer was used to identify the crystalline phases. CuKα radiation was used and the XRD pattern was obtained by scanning from 5 to 60 degrees. The components of the sample were identified by comparing with the standards established by the International Center for Diffraction Data.

Chloride and sulfate richness over a cut surface from the outer region (surface of the specimen) to the center of the specimens was also evaluated by Electron Probe Micro Analyzer (EPMA). For this test (EPMA) concrete samples were cut, polished, cleaned and coated. The sample was cut by a low speed diamond cutter. The polishing was done successively from coarse to fine in four steps (3, 1, 0.3 and 0.05 micron) by Al_2O_3 powder. The cleaning was done by ultrasonic method keeping the specimen in propane. Finally, the sample was coated with platinium alloy before investigations.

The matrix portions (with and without pores) were investigated by SEM at the mid height of the specimens at the inner and outer regions. For this, the specimens were cut at the mid-height by a diamond saw and a disc of about 20 mm was collected. Later, fractured surfaces perpendicular to the height of the specimens were investigated at the outer (20 to 30 mm from the surface) and the inner (70 to 80 mm from the surface) regions of the specimens. Similarly, samples were taken to investigate the aggregate-matrix interfaces of the fractured surfaces located at the outer and the inner regions as before. In order to investigate the steel-matrix interfaces, the matrix portions surrounding the steel bars were split opened. Then the fractured surface (perpendicular to the bar) and the surface over the bar (split opened surface) were examined by SEM. All samples were carbon coated before SEM observations.

The distributions of CaO and chlorides over the aggregates are also examined by EPMA (Electron Probe Micro Analyzer) after cutting and polishing and cleaning the surfaces properly as mentioned earlier.

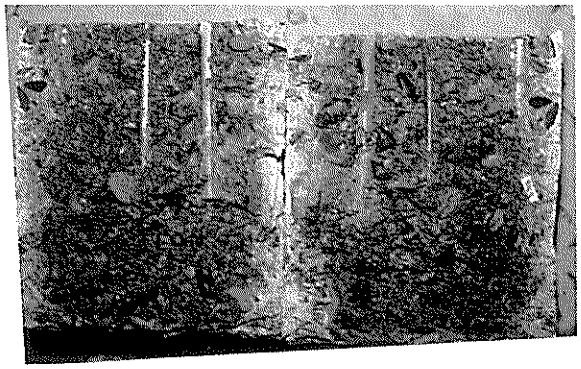

OPC

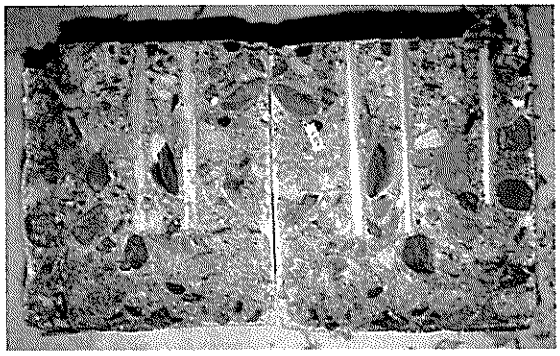

SCB

Fig. 4 Split Open Surface of the Specimens (Series 3)

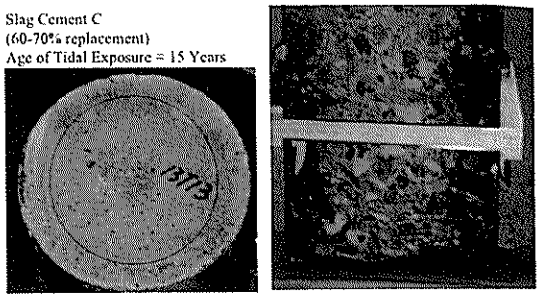

SCC

Fig. 5 Cut and Split Open Surface of the Specimens (Series 2)

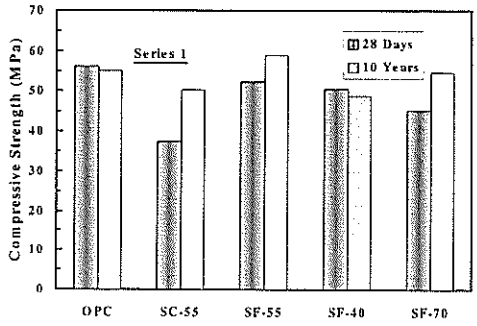

Fig. 6 Concrete Strengths at 28 Days and after 10 Years of Exposure

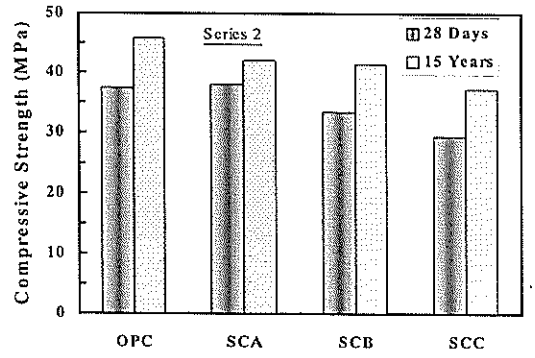

Fig. 7 Concrete Strength at 28 Days and after 15 Years of Exposure

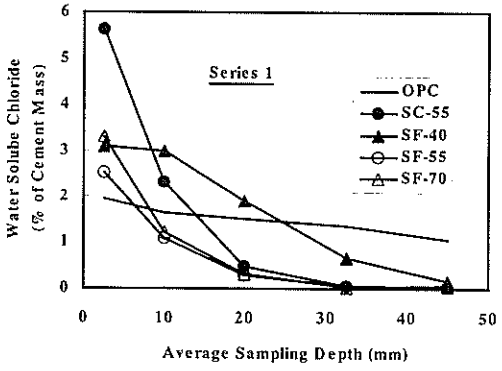

Fig. 8 Water Soluble Chloride Profiles (Series 1)

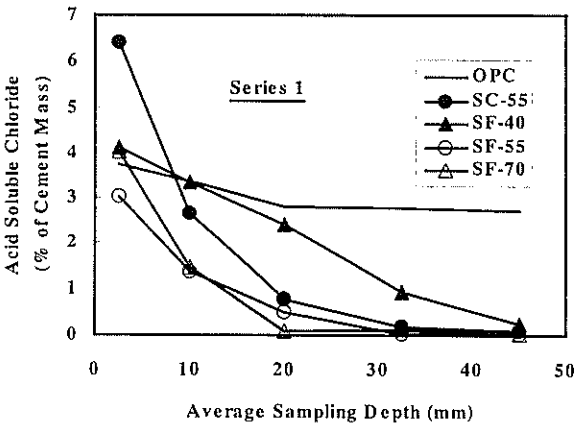

Fig. 9 Acid Soluble Chloride Profiles (Series 1)

3. Experimental Results and Discussion

3.1 Physical Observation and Water Content in Concrete

After 10, 15, and 30 years of exposure, no cracks were found over the concrete specimens due to the corrosion of the steel bars in concrete or any other chemical influence, such as formation of ettringite, alkali-silica reaction, etc. After splitting the specimens, it was remarkable that for OPC, the fractured surface was in wet condition, whereas for slag cements it was in dry condition. As an example, the fractured surfaces of Series 3 are shown in **Fig. 4** for SCB. The evaporable water content of concrete was measured after drying the samples in an oven at temperature 110°C for 24 hours. For OPC and SCB, the evaporable water content was 3.8% and 2.8%, respectively. The presence of a wet surface indicates lower concrete resistance and higher ingress of ions from seawater, such as chloride, sulfate, and others.

The cut surface of SCC for Series 2 is shown in **Fig. 5**. The presence of a dark blue, hard, and dense crust is developed for slag cement after 15 years of exposure. This was clearer for SCC, where the slag content was 60-70% of cement mass. The microstructural and mineralogical information of the outer and inner regions are explained later. The outer dense layer screens most of the chloride at the outer region. Explanations about the chloride ingress are provided later.

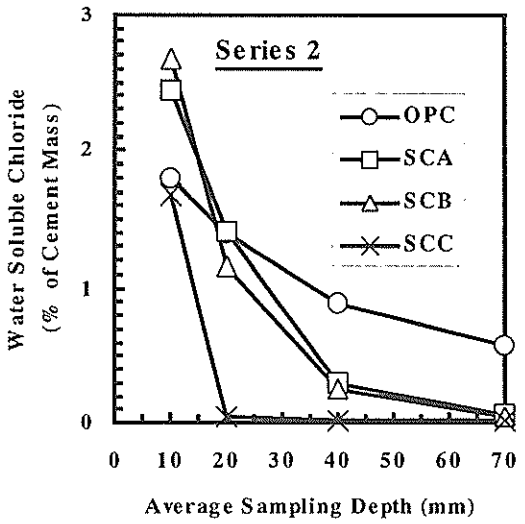

Fig. 10 Water Soluble Chloride Profiles (Series 2)

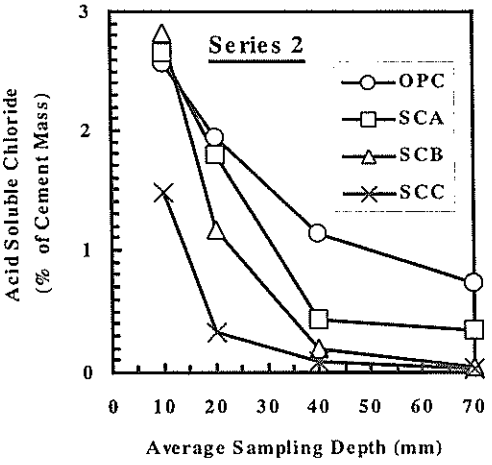

Fig. 11 Acid Soluble Chloride Profiles (Series 2)

3.2 Compressive Strength of Concrete at the Early Age and Long-Term of Exposure

Compressive strength of concrete at the age of 28 days and after 10 years of tidal exposure is shown in **Fig. 6**. It is found that for course slag (SC-55), the early age of compressive strength is relatively lower compared to the OPC and fine slag (SF-55). It is due to the slow rate of hydration for coarse slag. However, the long-term strength gain is much better for coarse slag compared to fine slag. The strength gain for OPC is not so significant compared to the slag cements. It is also realized that the more the slag contents the more is the later strength gain (SF-40, SF-55, SF-70). However, 55% replacement (SF-55) shows maximum strength compared to 40% and 70% of replacements.

Compressive strength of concrete at the 28 days and after 15 years of exposure in tidal environment for Series 2 is shown in **Fig. 7**. Same as Series 1, it is found that for slag cements the early strength is relatively lower compared to OPC. Slag cement with more slag contents (SCC) also shows lower strength at the early age compared to the slag cement with less slag content (SCA, SCB). However, the more is the slag content the more is the later strength gain.

From these long-term data, it is clearly understood that if the designer can satisfy the required 28 days strength by using slag cement, it is prudent to use slag cement. It will gain strength gradually and after a long-term of exposure it will provide an additional strength compared to the 28 days strength. In addition, it will reduce the chloride ingress in concrete as explained below.

3.3 Carbonation Depths and Chloride Diffusion in Concrete

Carbonation depths of concrete were negligible irrespective of all series of the specimens. Therefore, corrosion over the steel bars explained here will be limited to the chloride-induced corrosion. Water- and acid-soluble chloride profiles for Series 1 are shown in **Figs. 8 and 9.** After 10 years exposure, the chloride concentrations at the center region of the specimens for OPC become more than 1% of cement mass, however it is much lower than 0.4% of cement mass for slag cements, irrespective of the slag contents and slag fineness. Generally, chloride concentration of 0.4% of cement mass defines as chloride threshold value. For slag cements, surface chloride concentration is higher than the same for OPC. For slag cements, the chloride level just reaches the chloride threshold level at the 20 mm of cover depths, however at the 40 mm of cover depths it is much lower than the chloride threshold level. The results clearly indicate that if a structure is designed with OPC, after ten years of exposure the chloride level at the steel level will exceed the chloride threshold within ten years, even for a cover depths more than 50 mm. Same kind of results were also observed in splash exposure. The results can be obtained in **Reference 13**. The diffusion coefficient and the time to initiate corrosion are discussed later.

Water- and acid soluble chloride profiles after 15 years of exposure (Series 2) are shown in **Figs. 10 and 11**. Same as Series 1, slag cements reduce the chloride ingress in concrete. The more is the slag content the less is the chloride ingress. A tendency of having much chloride at the surface region is found for slag cements. After 15 years exposure, chloride level at 20, 40, and 70 mm of cover concrete crosses the chloride threshold level for OPC. However for SCC (60 - 70% slag content), the chloride level was even lower than the threshold level at cover depths of 20 mm. Same as Series 1, the results clearly indicate that the slag cements are very useful for the reduction of chloride ingress in concrete.

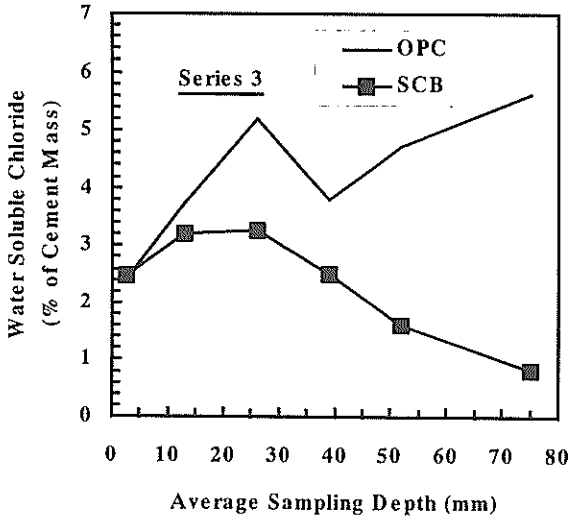

Fig. 12 Water Soluble Chloride Profiles (Series 3)

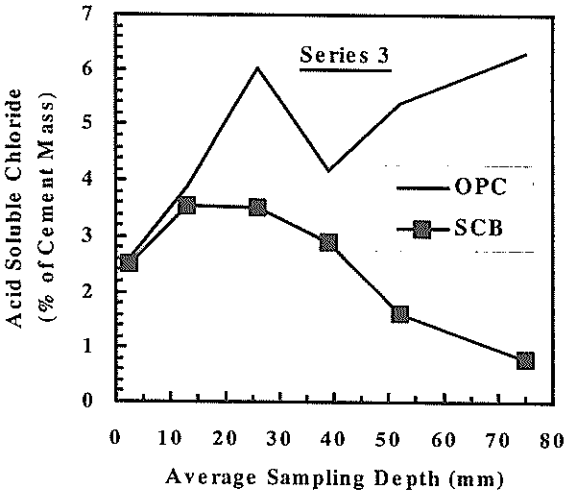

Fig. 13 Acid Soluble Chloride Profiles (Series 3)

Table 13 Diffusion Coefficient and Time to Initiate Corrosion

Series	Specimen	Diffusion Coefficient (mm^2/year)	Time to Initiate Corrosion (year)
1	OPC	192	8
	SC-55	7	108
	SF-40	36	29
	SF-55	8	150
	SF-70	7	136
2	OPC	75	22
	SCA	16	19
	SCB	12	98
	SCC	8	150

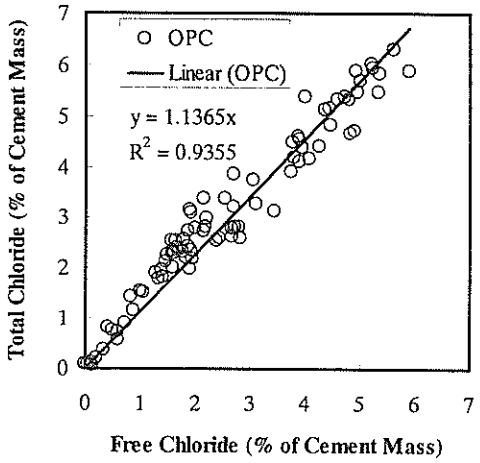

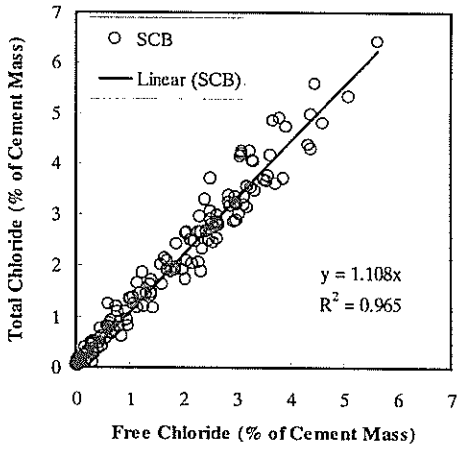

Fig. 14 Total Chloride and Free Chloride (Top: OPC, and Bottom: SCB)

Water- and acid-soluble chloride profiles after 30 years of exposure are shown in **Figs. 12 ~ 13**. Same as Series 1 and Series 2, it is found that for slag cement chloride ingress is much lower than that of the OPC. After 30 years of exposure, the chloride level at the center region of the specimens crosses the threshold limit of chloride for slag cement. For OPC, at the center region, the chloride level is much higher than the outer regions. It is because of the circular shape of the specimens as well as leaching of chloride from the surface region of the specimen due to the change in microstructure of the outer region.

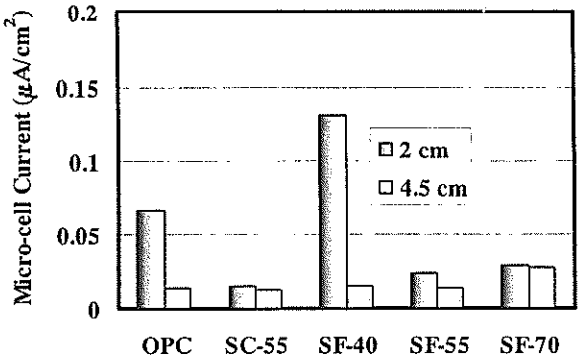

Fig. 15 Micro-Cell Corrosion Over the Steel Bars (Series 1)

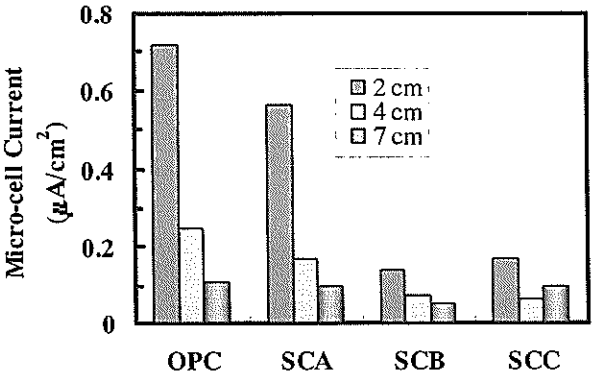

Fig. 16 Micro-cell Corrosion Over the Steel Bars (Series 2)

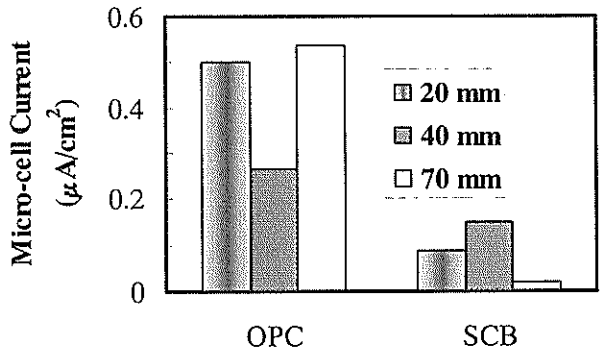

Fig. 17 Micro-Cell Corrosion Over the Steel Bars (Series 3)

3.4 Diffusion Coefficient and Time to Initiate Corrosion

Chloride diffusion coefficient was calculated based on the water-soluble chloride profiles explained before. The calculated diffusion coefficients are given in **Table 13**. The diffusion coefficient is much higher for OPC compared to slag cements. No significant influence of slag fineness is found after long-term of exposure. The more is the slag content, the less is the diffusion coefficient.

Time to initiate corrosion was calculated based on the chloride threshold level at 0.4% of cement mass, and cover concrete depth of 70 mm. The time to initiate corrosion for OPC is found to be around 10 years, however the figure becomes more than 100 years, especially for a higher amount of slag content (SC-55, SF-55, SF-70, SCC). The results clearly indicate that chloride ingress can be significantly reduced by using slag cements with a high amount of slag content (about 55% or more).

3.5 Relationship Between Water and Acid Soluble Chlorides in Concrete

Acid-soluble chloride versus water-soluble chloride is plotted in **Fig. 14** for OPC, and SCB. All other available data at the author's hand on the long-term exposure experiments are incorporated here. The amount of bound chloride (*BC*) can be correlated with the water-soluble chloride (*WSC*) by the following equations for OPC and SCB:

$$\textit{For OPC,}\quad BC = 0.137WSC \tag{5}$$

$$\textit{For SCB,}\quad BC = 0.108WSC \tag{6}$$

It is found that the amount of bound chloride (BC) (difference between the acid- and water-soluble chlorides) of concrete made with slag cement is lower than OPC. It indicates that for the same amount of total chlorides, the amount of bound chloride will be less for slag cements. Generally, the bound chloride has no influence on the breakdown of the passivation film over the steel bars. The less chloride binding ability of concrete made with slag cement does not necessarily indicate more corrosion, as the chloride ingress in concrete made with slag cement is much lower compared to the OPC, as explained before.

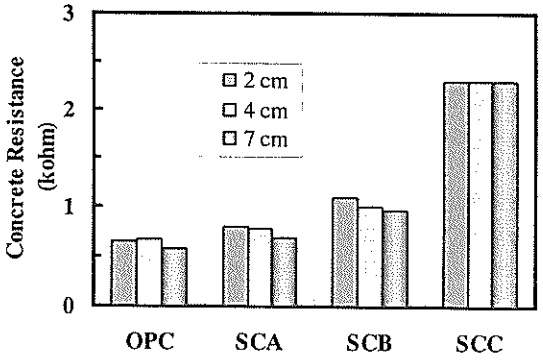

Fig. 18 Concrete Resistance (Series 2)

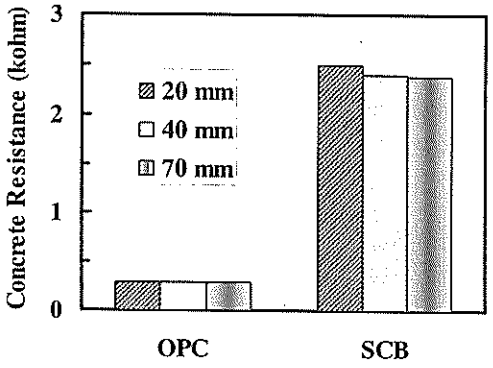

Fig. 19 Concrete Resistance (Series 3)

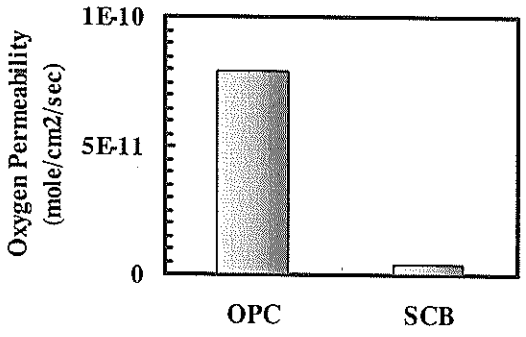

Fig. 20 Oxygen Permeability (Series 3)

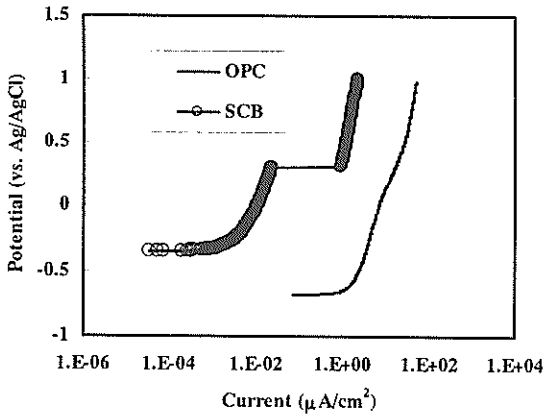

Fig. 21 Anodic Polarization Curves (Series 3, 20 mm Cover)

Table 14 Passivity Grades (Series 1)

Specimens	Passivity Grades	
	20 mm Cover	45.5 mm Cover
OPC	4	3
SC-55	4	5
SF-40	4	4
SF-55	3	4
SF-70	4	4

Table 15 Passivity Grades (Series 2)

Specimens	Passivity Grades		
	20 mm	40 mm	70 mm
OPC	3	3	4
SCA	3	4	4
SCB	4	4	4
SCC	3	4	4

Table 16 Passivity Grades (Series 3)

Specimens	Passivity Grades	
	20 mm	70 mm
OPC	1	1
SCB	4	4

3.6 Micro-cell Corrosion of Steel Bars in Concrete

Micro-cell corrosion current density over the steel bars is shown in **Fig. 15, 16, and 17** for Series 1, 2, and 3, respectively. For Series 1, the micro-cell current density is less than 0.1 $\mu A/cm^2$ in many cases, which indicates that the good passivity over the steel bars is remained even for a chloride concentration more than 2% of cement mass (**14**). In Series 1, a special method was adopted during

casting concrete, which leads to develop a good steel-concrete interface, and thereby prevents the initiation of corrosion even for chloride concentration more than 2% of cement mass over the steel bars. This matter is discussed later in a separate sub-section.

For Series 2, the micro-cell corrosion over the steel bars crosses the passivity limit of 0.1 $\mu A/cm^2$, which indicates the possibility of corrosion over the steel bars. For OPC, the current density is higher than the slag cements. The more is the slag content the less is the current density. For Series 2, it is also found that the corrosion current density over the steel bars for OPC is much higher than the same for slag cement. The steel bars in concrete made with slag cements seem to be in passive condition after 10, 15, or 30 years of exposure, especially for the cases with more slag content. These results clearly indicate that the utilization of slag cement is very useful to reduce the corrosion of steel bars in concrete under marine environment.

3.7 Concrete Resistance and Oxygen Permeability Through Concrete

Concrete resistance over the different cover concrete for Series 2 and 3 are shown in **Fig. 18 and 19**. For slag cements, the concrete resistance is several times higher than the same for OPC. A higher concrete resistance indicates denser microstructure of concrete. It is already explained before that after split open the specimens, the presence of clear water is found for OPC inside the specimens, however for slag cements the inner region remains dry even after 30 years of exposure (**Fig. 4**). A higher concrete resistance also indicates lower corrosion activity by reducing the movements of ions in concrete.

Oxygen permeability through the cover concrete for Series 3 (Cover Concrete = 40 mm) is shown in **Fig. 20**. It is found that oxygen permeability is about 20 times higher for OPC compared to the SCB. The results matched well with concrete resistance data as well as the chloride ingress, and micro-cell corrosion over the steel bars.

3.8 Anodic Polarization Curves and Passivity Grades of Steel Bars in Concrete

The anodic polarization curves of steel bars at cover depth of 20 mm for Series 3 are shown in **Fig. 21**. It is found that the anodic polarization curve is far away from the potential axis for OPC compared to SCB. It indicated that a stronger passivity over the steel bars for SCB.

The passivity grades of the steel bars were evaluated in a scale of 0 to 5 based on **Reference 9**. The more is the number the better is the passivity, i.e., the lower is the corrosion susceptibility. The passivity grade 0 means complete loss of passivity and 5 means excellent passivity. The passivity grades for Series 1, 2, and 3 are given in **Tables 14, 15, and 16**. For Series 1, relatively stronger passivity grades are observed irrespective of the cement types. This is due to a very special method of casting concrete that leads to an improvement of steel-concrete interface, and thereby protecting the steel bars from corrosion even for a chloride concentration more than 2% of cement mass. The method of casting concrete is explained later. In general, a higher degree of passivity is observed for slag cements compared to the OPC. The results clearly indicate that the steel bars in concrete made with slag cements have less corrosion susceptibility than OPC.

Table 17 Water Soluble Chloride Ion Concentrations at the Cracked and Uncracked Regions

Specimen	Crack Widths (mm) and Water Soluble Chloride Ion Concentrations (wt. % of C) *		
	1	2	3
OPC	0.2 (1.28) ((1.27))	0.1 (1.14) ((0.64))	0.1 (1.38) ((1.41))
SCA	0.1 (0.33) ((0.17))	0.3 (0.78) ((0.23))	0.2 (0.49) ((0.43))
SCB	0.3 (0.45) ((0.31))	0.1 (0.41) ((0.28))	*5* *(3.2)* *((0.16))*
SCC	*1.5* *(1.67)* *((0.19))*	0.1 (0.37) ((0.23))	*2* *(1.84)* *((0.69))*

*The figures in (.) and ((.)) indicate chloride ion concentration at cracked and uncracked regions respectively. The figures without bracket indicate crack widths. Wider cracks (Unhealed cracks) are noted as bold-italic letters.

Table 18 Crack Widths, Microcell Current Density and Extent of Corrosion of Steel Bars at the Cracked Region

Specimen	Crack Widths (mm) and Microcell Current Density ($\mu A/cm^2$)		
	1	2	3
OPC	0.2 (0.25) L	0.1 (0.24) L	0.1 (0.47) L
SCA	0.1 (0.25) L	0.3 (0.34) L	0.2 (0.25) L
SCB	0.3 (0.25) L	0.1 (0.15) L	*5* **(1.71)** H**
SCC	***1.5*** **(1.08)**** **H**	0.1 (0.19) L	*2* **(1.29)** H**
FACB	0.1 (0.28) L	0.3 (0.39) L	0.5 (0.52) M

*The figures in the brackets indicate microcell current density in $\mu A/cm^2$. The figure without brackets indicate crack width in mm. Bold-italic figures indicate wider or unhealed crack. L, M, H represent the extent of corrosion as low, moderate and high respectively. **Bottle-neck formed due to the corrosion around the perimeter of the bar.

3.9 Chloride Concentrations and Micro-Cell Corrosion – Cracked Concrete

Cracked prism specimens were investigated for Series 2 only. Water-soluble chloride concentrations of prism specimens at the cracked and uncracked regions are listed in **Table 17.** Relatively less chloride concentration is observed at the uncracked region. In the case of wider cracks, significant amount of chloride concentration is observed at the cracked region. This is expected to be more in the case of slag cements due to the accumulation of more chloride in concrete at the unhealed cracks. For narrower crack widths, slag cements, especially SCC shows the best performance against the chloride ingress in concrete. Chloride ingress in concretes with various cements is sequenced as OPC>SCA>SCB>SCC. SEM investigations on the healed cracks are explained later.

Microcell current density of the steel bars at the cracked region of prism specimens are listed in **Table 18** for different cements. For narrower crack widths, a tendency of having lower current density is observed. The extent of corrosion for the narrower cracks ($\leqq$0.5 mm) was also evaluated as low (**14**). It was found that after 15 years exposure, cracks were healed. Deposits were also seen over the debonded area of the steel bars near the cracks. Therefore, it is expected that the corrosion process is stopped or reduced significantly due to the healing. The degree of corrosion, can be sequenced as OPC>SCA>SCB>SCC for narrower crack widths.

Wider cracks (marked as bold-italic letters in **Table 18**) were not healed. Higher amount of micro-cell current density was also observed at the wider cracks. The extent of corrosion was evaluated as high for these cracks (**14**). Significant amount of corrosion around the perimeter of steel bar at the cracked region causes the formation of bottle-neck at the crack. It is widely known that the chloride-induced corrosion is autocatalytic. It lowers the pH value surrounding the steel bars and accumulates positive ions (Fe^{++}) at the cracked regions. The excess positive charges are balanced by the migration of chloride ions. It is clearly understood that in the case of narrower cracks, with the progress of crack healing this autocatalytic process is stopped or reduced significantly. On the other hand, the progress of the autocatalytic reaction continues in the case of wider cracks and leaded to the formation of bottle-neck due to the corrosion of steel bars along the perimeter. Very high amount of chloride ions at the cracked region also found at the wider cracks (**Table 17**).

3.10 Microstructures of Concrete – Porosity

The porosity of the mortar samples collected from the different depths of the specimens made with OPC and slag cements are shown in **Figs. 22~24.** It is found that after a long-term of exposure, the pore volume reduces or pore size shifts to smaller pores at the outer regions of the specimens. Shifting of the pore size to the finer pores results in the reduction of capillary pore volume. Generally, pore size from 0.01 – 1 μm is defined as the capillary pore (**15**). The volume of the capillary pores determines the permeability of ions in concrete. The reduction in pore volume is the most predominant for SCB and SCC. The more is the slag contents the more is the reduction in pore volume at the outer region of the specimens. The mineralogical compositions of the mortar samples at the different depths of the specimens are discussed later in order to clarify the reduction in pore volume. To compare the different cements, the pore size distributions of the different cements at depths of 5-15, 35-45 and 65-75 mm are shown in **Fig. 23.** It is clear that the microstructure of concrete with SCC is significantly improved compared to the others. The improvement is clearer at the outer region of the specimens. Based on these results, the condition (compactness) of microstructure of concrete at the outer regions of the specimens after 15 years of exposure is sequenced as SCC>SCB>SCA>OPC, i.e., the microstructure of concrete with SCC is better than the same with SCB and so on.

In the previous section, chloride ingress in concrete is sequenced as OPC>SCA>SCB>SCC. The results are matched with the pore size data. The use of slag cements creates a barrier against the chloride ingress due to the relatively inherent denser microstructure as well as the further reduction in pore volume at the outer region of the specimens. The reduction in pore volume at the outer region will also cause to reduce the connectivity of the capillary pore channels.

3.11 Mineralogy of Concrete

Mineralogy of the mortar samples at depths 5-15 mm from the surface of the specimens is shown in **Table 19** for Series 1. No ettringite is found for SCB, also the peaks for Friedel's salt are not so prominent.

The XRD results at the different depths of the specimens are summarized in **Table 20** for Series 2. Ettringite peaks are observed at the outer region (5-15 mm) of the specimens irrespective of the cement types investigated here. It is expected that the monosulfate hydrate transfers to the ettringite due to the infiltration of sulfate ions from the seawater as below (15).

$$MgSO_4 + \left[Ca(OH)_2 + 3CaO.Al_2O_2.CaSO_4.18H_2O\right] \rightarrow Mg(OH)_2 + 3CaO.Al_2O_3.3CaSO_4.32H_2O$$

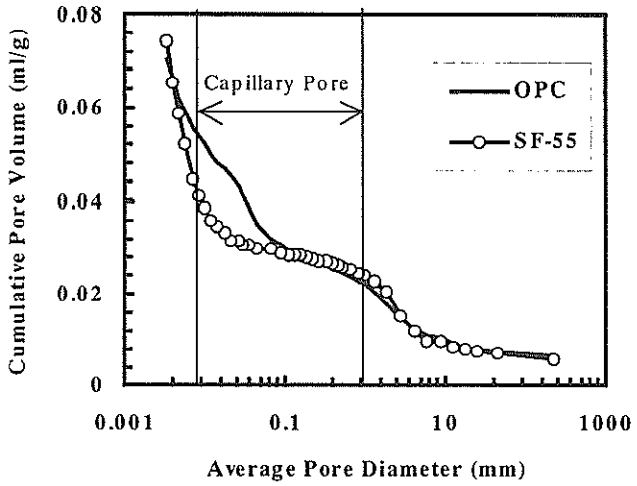

Fig. 22 Porosity of Mortar Samples (Series 1)

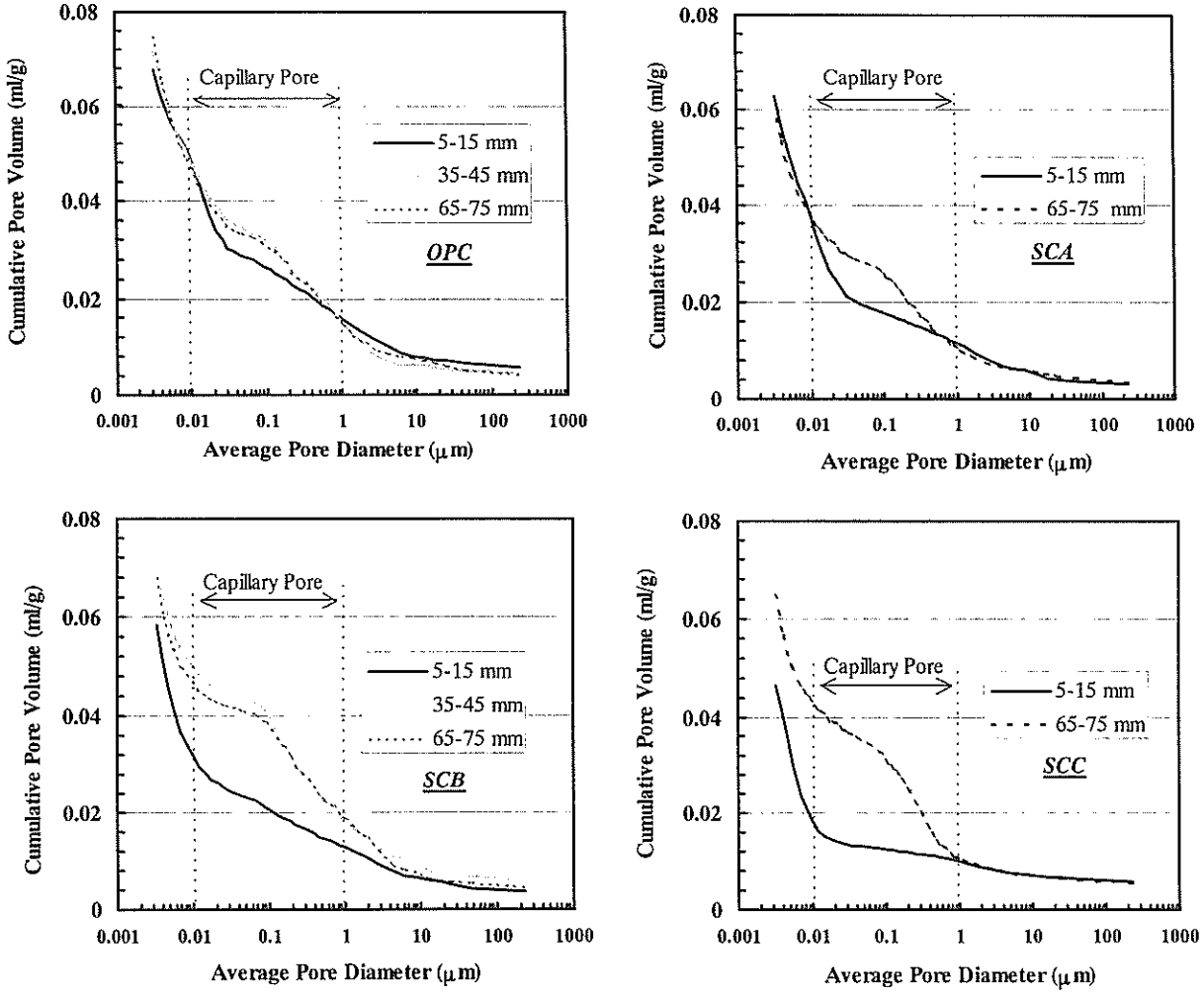

Fig. 23 Porosity of the Mortar Samples (Series 2)

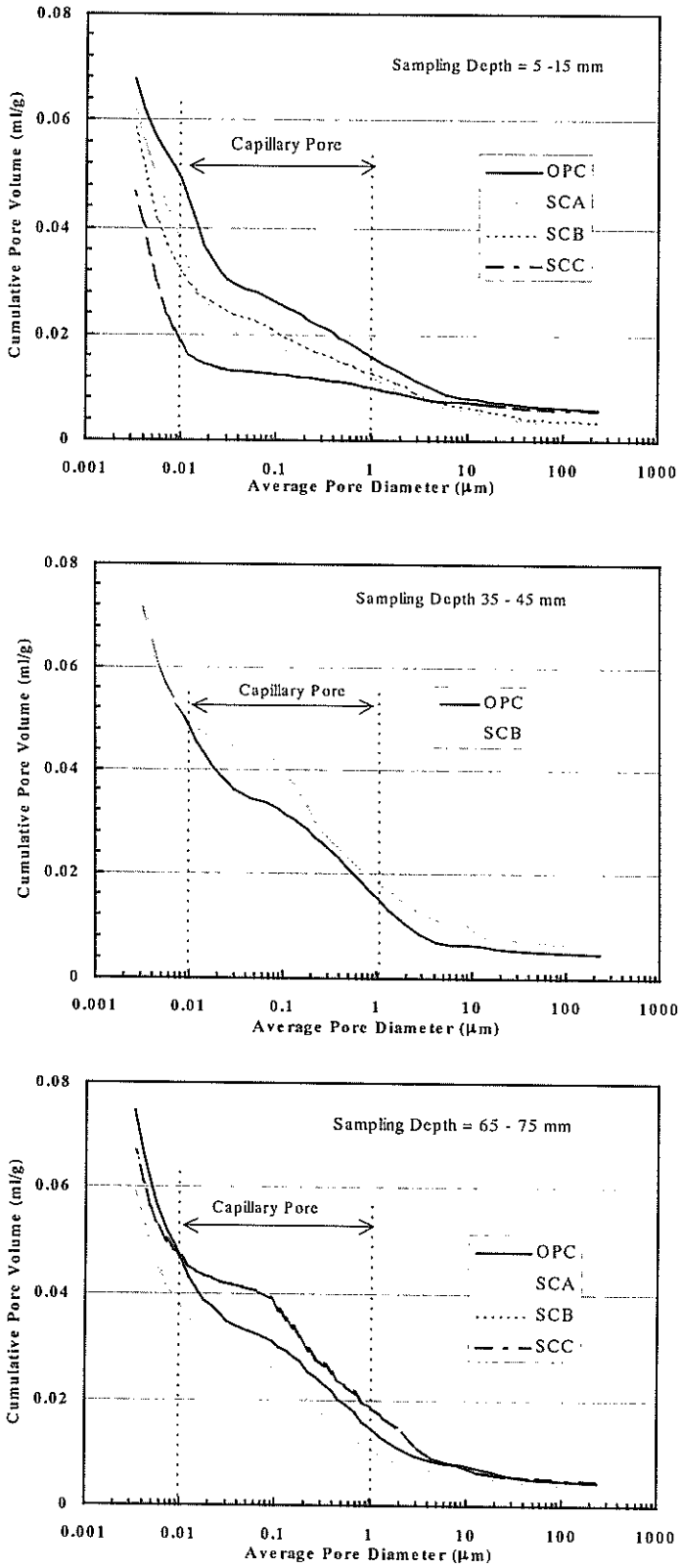

Fig. 24 Comparison of Porosity at the Different Depths for Different Cements (Series 2)

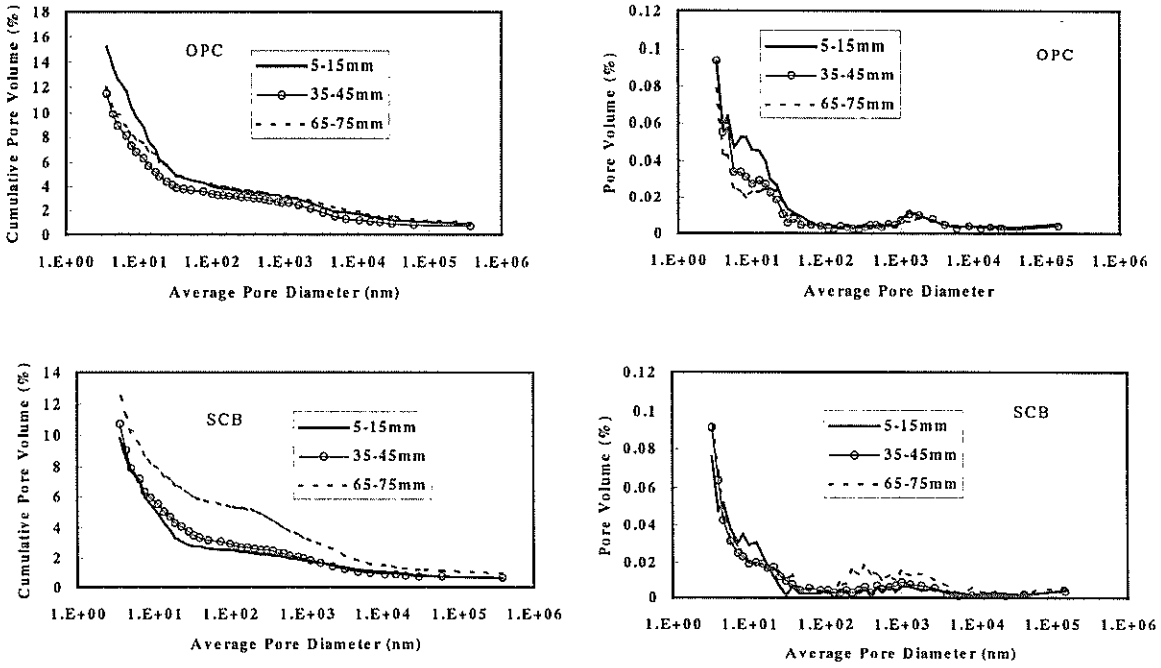

Fig. 25 Porosity at the Different Depths (Series 3)

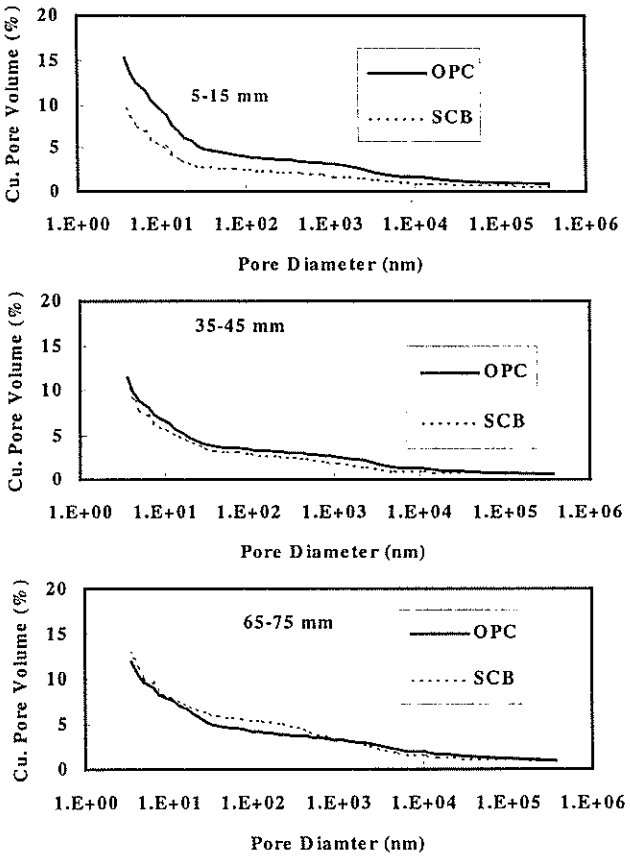

Fig. 26 Comparison of Porosity for OPC and SCB (Series 3)

Table 19 Summary of the XRD Data (Series 1, 15 – 25 mm from the surface)

Mineralogy	OPC	SF-55
$Ca(OH)_2$ (Calcium Hydroxide)	O	O
$3CaO.Al_2O_3.3CaSO_4.32H_2O$ (Ettringite)	△	-
$3CaO.Al_2O_3.CaCl_2.11H_2O$ (Friedel's Salt)	O	△
$CaCO_3$ (Calcite)	△	O

"O" means clearly observed, and "△" means observed but not so clear, "-" means not observed.

Table 20 Summary of the XRD Data (Series 2)

Compositions	OPC			SCA		SCB			SCC	
	5-15 mm	35-45 mm	65-75 mm	5-15 mm	65-75 mm	5-15 mm	35-45 mm	65-75 mm	5-15 mm	65-75 mm
$3CaO.Al_2O_3.CaCl_2.11H_2O$ (Friedel's Salt)	O	O	-	O	O	O	-	-	O	-
$Ca(OH)_2$ (Calcium Hydroxide)	O	O	O	O	O	O	O	O	-	O
$Mg(OH)_2$ (Magnesium Hydroxide)	O	-	-	-	-	-	-	-	-	-
$3CaO.Al_2O_3.3CaSO_4.32H_2O$ (Ettringite)	O	-	-	O	-	O	O	-	O	-
$3CaO.Al_2O_3.CaSO_4.12H_2O$ (Monosulfate)	-	O	O	-	O	-	O	O	-	O

"O" means observed, and "–" means not observed.

Table 21 Summary of the XRD Analysis at Inner (65-75 mm) and Outer (5 –1 15 mm) Regions

Mineralogy	OPC		SCB	
	Out.	In.	Out.	In.
Calcium Hydroxide Ca(OH)2	×	×	×	O
Magnesium Hydroxide Mg(OH)2	×	×	×	×
Ettringite 3CaO.Al2O3.3CaSO4..32H2O	O	O	O	Δ
Calcium Carbonate CaCO3	×	×	×	×
Friedel's salt 3CaO.Al2O3.CaCl2.10H2O	O	O	O	Δ
Calcium Silicate Hydrate nCaO.SiO2.mH2O(n=1.2-2.0)	Δ	Δ	Δ	Δ
Monosulfate 3CaO.Al2O3.CaSO4.12H2O	×	×	Δ	Δ

○ : Clearly Observed Δ : Not Clearly Observed, × : Not Observed

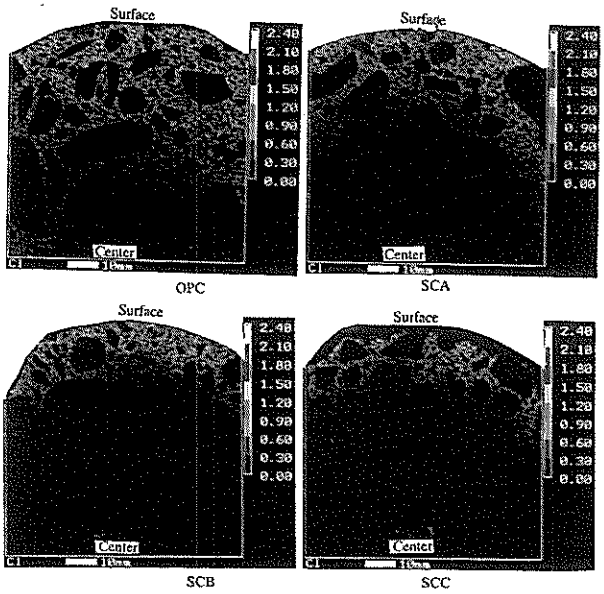

The scale at the right indicates chloride richness qualitatively.

Fig. 27 Distribution of Cl^- on the Polished Surface (Series 2)

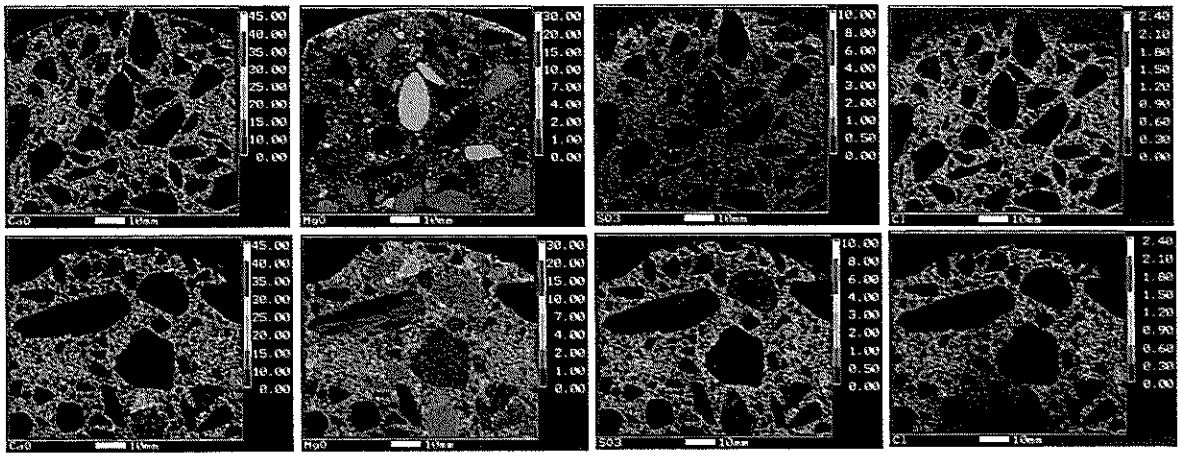

CaO MgO SO_3 Cl

Scale at the right indicates the richness of investigated items qualitatively.

Top Row – OPC, Bottom Row – SCB

Fig. 28 Distribution of CaO, MgO, SO3, and Cl- from the Surface to the Inner Region (Series 3)

The absence of the monosulfate peaks at the outer region of the specimens (5 to 15 mm) irrespective of the cement types can be explained with the above-mentioned reason. The monosulfate is generally observed at the inner portion of the specimens irrespective of the cement types. $Mg(OH)_2$ is observed at the outer region of the specimens (5-15 mm) with OPC. It is expected to produce with ettringite due to the reaction of magnesium sulfate with monosulfate and calcium hydroxide. Other possible reactions to form the magnesium hydroxide are given below (**15**). It is understood that in the case of slag cements, the reaction of sea salts with the hydration products of cements is only limited to the outer regions. This can be again explained due to the improvement in microstructures of concrete as before.

$$MgCl_2 + Ca(OH)_2 \rightarrow Mg(OH)_2 + CaCl_2$$

$$MgSO_4 + Ca(OH)_2 \rightarrow Mg(OH)_2 + CaSO_4.2H_2O$$

$$MgSO_4 + [Ca(OH)_2 + 3CaO.2SiO_2.3H_2O] \rightarrow 4MgO.SiO_2.8H_2O + CaSO_4.2H_2O$$

The presence of $Ca(OH)_2$ is recognized at the outer and inner regions of the specimens irrespective of the cement types, except SCC. The peak was low at the outer regions compared to the inner regions. For SCC, it is not recognized at the outer region. The results indicate that the above-mentioned reactions may occur in some extent. As the calcium chloride and calcium sulfate are water soluble, therefore, it results in material loss and weakening. However, in this investigation, it is not found. The concrete at the outer region even becomes denser than the inner region.

More clear peaks of Friedel's salt are observed in the case of OPC up to a depth of 45 mm from the surface. The peaks were less clear for slag cements and only limited to the surface region.

For the further explanation of the reduction in pore volume with the use of slag cements, SEM micrographs were investigated for the matrix portion of concrete with and without pores. Also, aggregate-matrix and steel-matrix interfaces in concrete are investigated by SEM and EPMA. The results are explained later.

The mineralogy of the mortar samples of Series 3 are summarized in **Table 21**. $Ca(OH)_2$ peaks were only observed for SCB at the inner region. Ettringite peaks were clearly observed for OPC and at the outer region for SCB. For SCB, at the inner region, the ettringite peaks were not so clear. The same results are also observed for Friedel's salt peaks. Mnosulfate peaks were not observed for OPC. For SCB, the monosulfate peaks were not so distinct and can be explained as the transformation to the ettringite for OPC.

Chloride richness on a polished surface (Series 2) from the outer to the inner region is shown in **Fig. 27**. Least chloride ingress is clearly observed at the inner region for slag cements, especially SCC.

The distribution of calcium oxide, magnesium oxide, chloride, and sulfate on polished surfaces are shown in **Fig. 28**. It can be realized that for a thin surface region, calcium leaching is occurred, which is about 2 mm for OPC and SCB. MgO is observed over a thin surface layer around the specimens for OPC and SCB. For OPC, sulfate infiltrates around 7 mm from the surface region of the specimen. In the case of SCB, it is around 5 mm from the surface.

In the case of OPC, higher chloride concentration is not observed over the surface region. Higher chloride concentration is observed at the center region of the specimen. Less chloride concentration around the surface region is supposed due to the carbonation at the outer region as well as leaching of calcium. The carbonation depth for OPC was 5 mm and SCB 2 mm. In the case of SCB, low chloride level is observed over a thin surface region and then it gradually reduces toward the center region. Quantitative chloride data (acid and water soluble) are explained before. Quantitative chloride data match with the EPMA data. Same as before, less chloride ingress is concluded for SCB compared to OPC.

3.12 Microstructures of Concrete (SEM) – Series 2

The microstructure (SEM micrographs only) of matrix with and without pores is explained in two separate sub-sections. The location of the matrix is considered as outer (20 to 30 mm from the surface) and inner (70 to 80 mm from the surface) regions. The pore structures of concrete at the different depths of the specimens are explained before.

3.12.1 Matrix Without Pore

Typical Scanning Electron Micrographs of paste portions at the outer and inner regions are shown in **Fig. 29**. Irrespective of the type of the cements, and the inner and outer regions, dense morphology of C-S-H is observed. Randomly distributed CH crystals are also observed. The XRD charts showed the stronger peak of CH at the inner region compared to the outer region of the specimens. It indicated that the inner region is more lime rich compared to the outer region of the specimens. No significant deterioration of matrix is observed irrespective of the cement types after 15 years of exposure.

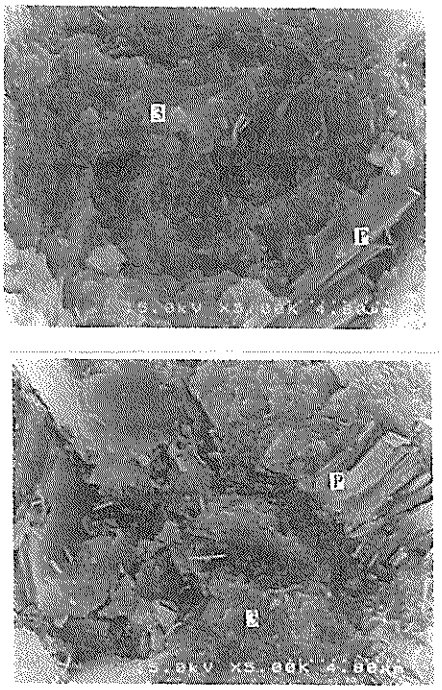

3 – Dense C-S-H, P – $Ca(OH)_2$

Fig. 29 SEM Micrograph of Matrix without Pore – OPC (Top : Outer Region, Bottom : Inner Region)

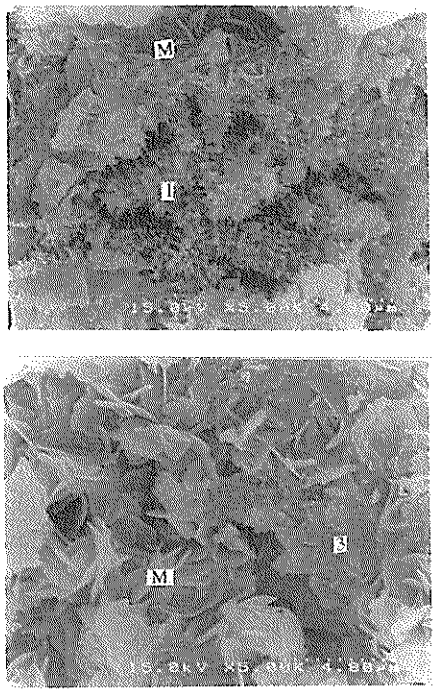

1- Porous C-S-H, 3 – Dense C-S-H, M – Monosulfate Hydrate

Fig. 30 SEM Micrograph of Matrix with Pore – Outer Region (Top : OPC, Bottom : SCB)

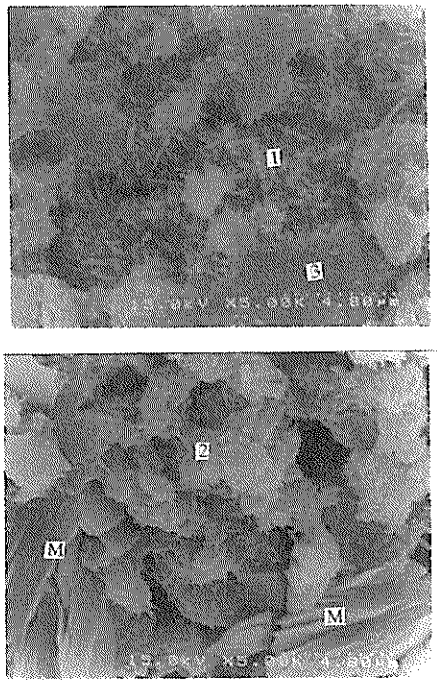

1,2 – Porous C-S-H, 3 –Dense C-S-H, M-Monosulfate, E - Ettringite

Fig. 31 SEM Micrograph of Matrix with Pore – Inner Region (Top : OPC, Bottom : SCB)

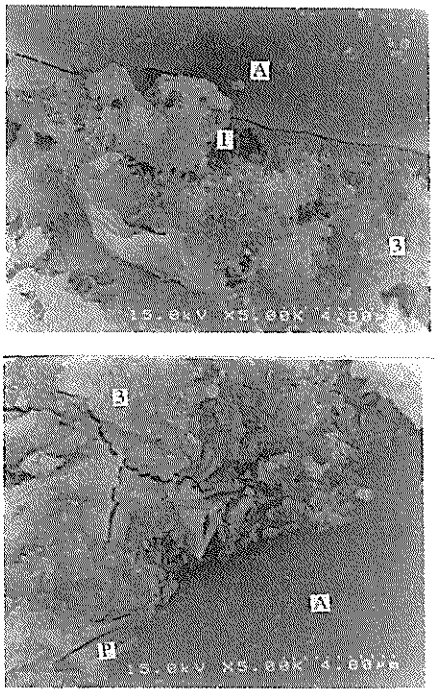

1- Porous C-S-H, 3 – Dense C-S-H, P – $Ca(OH)_2$, A - Aggregate

Fig. 32 SEM Micrograph of Matrix with Pore – Inner Region (Top : OPC, Bottom : SCB)

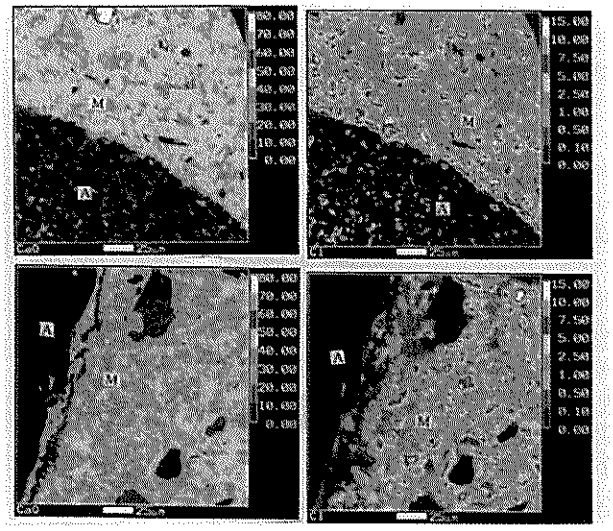

A : Aggregate, M – Matrix
The scale demotes the richness of chloride qualitatively.

Fig. 33 Distribution of CaO and Cl^- Over the Aggregate – Outer Region (Top: OPC, Bottom: SCB)

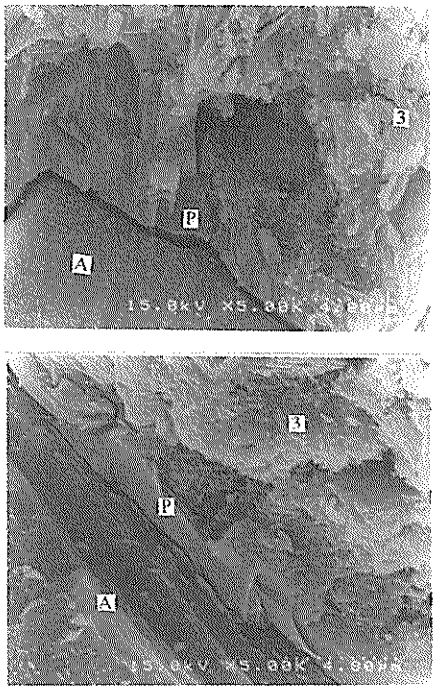

1-Porous C-S-H, 3 – Dense C-S-H, P – $Ca(OH)_2$, A - Aggregate

Fig. 34 SEM Micrograph of Aggregate-Matrix Interface – Inner Region (Top : OPC, Bottom : SCB)

3.12.2 Porous Matrix

Scanning Electron Micrographs of typical porous regions of the matrix located at the outer region are shown in **Fig. 30**. Porous C-S-H is observed in the case of OPC. The most important observation is that the denser morphology of C-S-H is clearly observed for slag cements. Also, densely populated monosulphate hydrate is observed in the pores. The results indicate that at the outer region of the specimens, the microstructure of concrete made with SCB and SCC is denser than that of OPC. Furthermore, with the long-term exposure, the microstructure of concrete at the outer region densified significantly compared to the inner region. Consequently the porosity is reduced and the pore size distribution is shifted to smaller pores as explained before. It will cause to reduce the interconnectivity of the pore channels of the hydration products. As a result, blocking of chlorides at the outer surface region, especially for the specimens made with SCB and SCC are clearly found, which is also explained before.

Typical Scanning Electron Micrographs of porous matrix at the inner regions are shown in **Fig. 31**. Same as before, in the case of OPC, the inner regions show the presence of porous C-S-H. In the case of slag cements, monosulphate hydrate is observed in the inner region, but it is not as denser as the outer regions. It indicates that after 15 years of exposure seawater leads to improve the microstructure of concrete at the outer region. This is expected due to the deposition of Friedel's salt, magnesium hydroxide and ettringite, which are confirmed by XRD charts at the outer region of the specimens.

3.12.3 Aggregate-Matrix Interface

Same as before, aggregate-matrix interface is also explained at the outer (20 to 30 mm from the surface) and the inner (70 to 80 mm from the surface) regions of the specimens separately.

Typical aggregate-matrix interfaces at the outer region are shown in **Fig. 32**. It is found that the CH crystals are not observed over the aggregate for OPC. Porous C-S-H is also found over the aggregate for OPC. These are expected due to the reason of calcium leaching as well as the reactions with the seawater and hydration products. In the case of SCB and SCC, randomly distributed crystals of CH are observed over the aggregate. Dense morphology of C-S-H products is also observed. The results suggest that the interfacial region at the outer region is more compact for SCB and SCC compared to OPC. The maximum thickness of the CH crystals is estimated at about 10 μm. As the micro-hardness of the interfacial zones were not evaluated, therefore, the accurate thickness of the weaker interfacial zone could not be evaluated.

The EPMA results of the distribution of CaO and chlorides on the polished surface over an aggregate located in between 5 to 10 mm from the surface of the specimen are shown in **Fig. 33**. It is important to note that in the previous section, the aggregate-matrix interfaces are explained for an aggregate located at 20 to 30 mm from the surface of the specimens. Irrespective of the cement types, higher concentration of CaO is not observed over the aggregate. It indicates leaching of calcium ions from the aggregate-matrix interface located very near to the surface of the specimen (5 to 10 mm from the surface). Chlorides are concentrated at the interfacial zone in the case of OPC and SCA. The removal of CH from the outer region (5 to 10 mm) of the interface is explained due to the leaching of the calcium ions. The probable reactions on this matter are explained before.

Typical aggregate-matrix interfaces at the inner region are shown in **Fig. 34**. Massive crystals of CH surrounding the aggregate are found for OPC. Dense C-S-H is observed irrespective of the type of the cement. The maximum thickness of the CH zone is estimated at around 10 μm as in the outer region. In the case of slag cements, the crystals are randomly distributed. However, in the case of OPC, the crystals are oriented almost in one direction, nearly perpendicular to the aggregate surface. The results indicate a compact interfacial zone in the case of slag cements, especially for SCB and SCC. This will cause to reduce the chloride ingress for these

cements as the interfaces are the weak link in concrete that help the migration of ions inside the concrete.

The distribution of CaO and chlorides over the aggregate are presented in **Fig. 35**. Irrespective of the cement types, CaO seems to be concentrated at some regions of the aggregate-matrix interface. Compared to the outer region, a little amount of chlorides is found over the aggregate in the inner region. Very little amount of chlorides is found for SCB. The results agree with the quantitative chloride analysis data explained before.

It is clearly understood that the aggregate-matrix interface is composed of CH and C-S-H. The same also observed in other studies (**16~18**). In this study, it is found that the use of slag cements, especially SCB and SCC reduces the preferential orientation of CH crystals over the aggregate that results in efficient packing near the interface.

3.12.4 Steel-Matrix Interface

Typical SEM micrographs of steel-matrix interfaces at the outermost (cover concrete depth = 20 mm) and the innermost (cover concrete depth = 70 mm) steel bars are shown in **Figs. A1~A4** (appendix attached at the end of the paper). It is found that irrespective of the depth of the cover and type of cements, a porous region is formed around the steel bar. The ettringite is also observed over the steel bars located at the outer region for the specimens made with OPC. The voids are supposed to be created due to the wall effect, i.e., packing of the cement grains around the steel bars (**19**). It results a porous region of the interconnected channels around the steel bar. The thickness of this region is estimated in the order of 50 μm.

The steel-matrix interface seems to be weaker (porous) than the aggregate-matrix interface. The same result was also concluded in the **Reference 17**, based on the micro-hardness values near the transition zones. It was found that the micro-hardness values measured over the aggregate-matrix interface are not so different from the same measured on the bulk matrix. However, significant difference was observed between the hardness values measured over the steel-matrix interface and bulk matrix. It was expected due to (1) the fixed nature of inclusion (the aggregate is allowed to move after casting in the plastic concrete) (2) smooth nature of inclusion and (3) mixing of inclusion during casting.

It is already noted that the micro voids are created over the steel-concrete interfaces irrespective of the type of the cements and the cover concrete depths. Therefore, techniques to improve the steel-concrete interfaces are necessary to be developed in order to enhance the long-term durability of concrete structures in the marine environment. With this improvement, the chloride threshold value against the onset of corrosion will be improved significantly.

The back-scattered electron images of the steel-concrete interface of the innermost steel bar are shown in **Fig. A5**. A porous zone of maximum thickness about 50 μm is clearly observed over the steel bars.

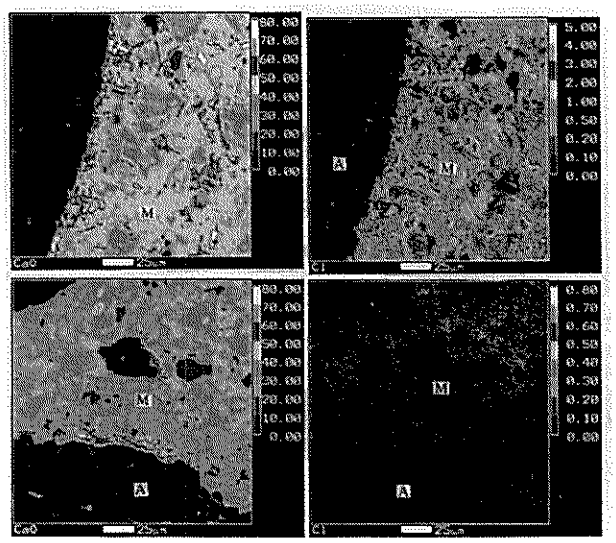

A : Aggregate, M – Matrix
The scale demotes the richness of chloride qualitatively.

Fig. 35 Distribution of CaO and Cl^- Over the Aggregate – Inner Region (Top: OPC, Bottom: SCB)

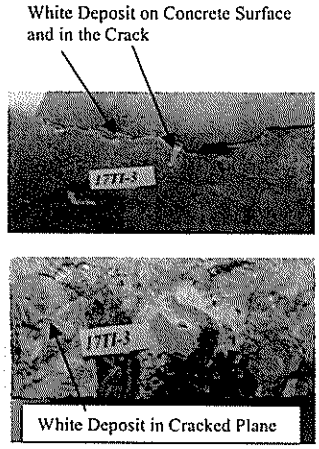

Photographs of Concrete Surface (top) and Cracked plane (bottom). Crack width at the surface is 0.5 mm.

Fig. 36 Photographs of a Healed Crack (Top – Concrete Surface, Bottom – Split Open Crack Plane)

3.13 Microstructures of Concrete (SEM) – Series 3

The results are discussed in the following four sub-sections, such as "Micro-Structure of Concrete at the Outer and Inner Regions", "Aggregate Matrix Interface", "Steel Matrix Interfaces", and "Healing of the Air Voids".

3.13.1 Micro-Structure of Concrete at the Outer and Inner Regions

Typical SEM micrographs of dense matrix located at 5~15 mm and 35~45 mm from the surface are shown in **Fig. A6**. Dense morphology of hydration products is observed. Dense hydration product is observed irrespective of the cases at the inner (5~15 mm) and outer regions (35~45 mm) of the specimens. However, the morphology of the hydration products for SCB is different from the OPC. For SCB, the hydration products seem denser compared to the OPC. Randomly distributed crystal of Friedel's salt was also observed in the matrix as shown in **Fig. A7**.

Typical SEM micrographs of the porous matrix at the inner (5~15 mm) and outer (35~45 mm) regions are shown in **Fig. A8**. It is important to note that the observed porous regions for SCB were less compared to the OPC. Deposition of Friedel's salt was also observed. Interestingly for slag cement, the morphology of hydration product was different from OPC. Relatively denser hydrates are found at the porous region for slag cement.

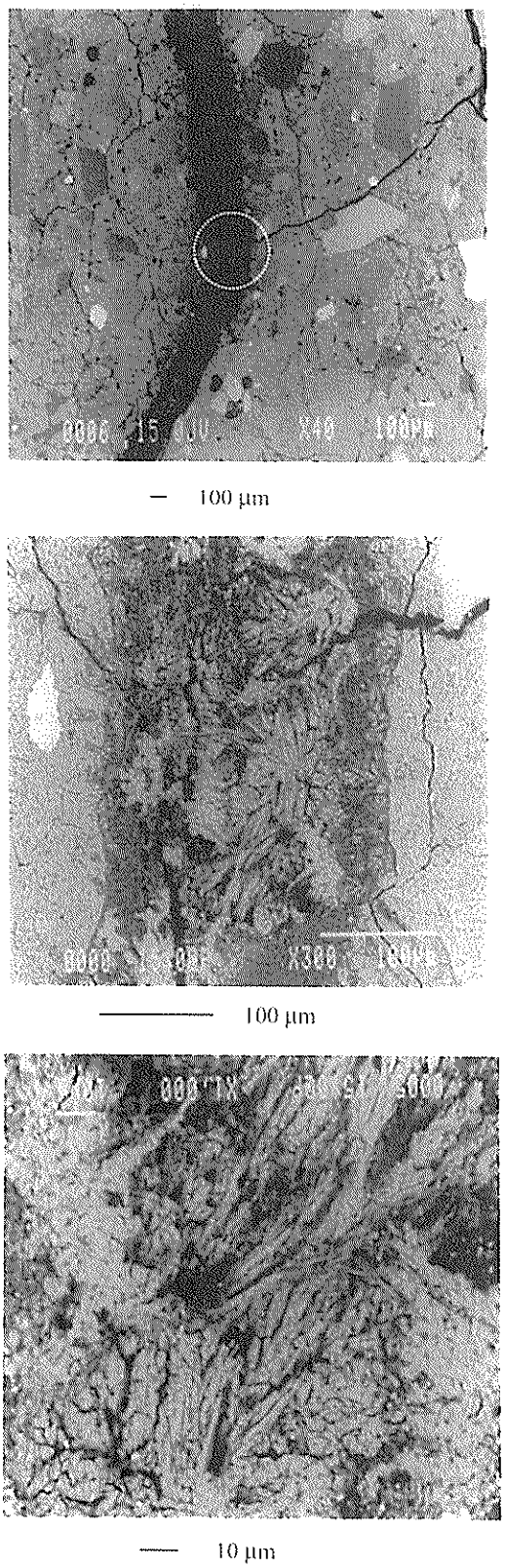

Sliced plane is located at 13 mm from the surface.

Fig. 37 Crack Healing (Crack Width =0.1 mm, SCB)

3.13.2 Aggregate-Matrix Interface

Typical SEM micrographs of the aggregate-matrix interface located at 5~15 mm and 35~45 mm from the surface of the specimens are shown in **Fig. A9**. The presence of $Ca(OH)_2$, CSH, and Friedel's salt were confirmed at the aggregate-matrix interface. Oriented $Ca(OH)_2$ deposits were also observed in some cases.

Interestingly, in the case of slag cement, the interface seems to be denser than OPC. The chloride diffusion also depends on the interfacial regions, as the interfaces are the weak links in concrete, therefore improved interfaces will cause to reduce the chloride ingress in concrete made with SCB. It was already explained before (Series 2) that the interfacial region is concentrated with relatively more chlorides compared to the bulk matrix. However, relatively less chloride was observed over the aggregate-matrix interface in concrete made with slag cement.

3.13.3 Steel-Matrix Interface

Steel-matrix interfaces were examined for the steel bar located at 40 mm of cover concrete only. The split open surface over the steel bars and the fractured surface normal to the steel bars are shown in **Fig. A10**. Generally, at the early stage of exposure, small pores were clearly observed over the steel bars, which size is expected to be similar to the mean cement particle size from 10 μm to 20 μm (**16**). These voids as well as other macro voids are healed in some extent after long-term of exposure due to the deposition of ettringite, monosulfate, and Friedel's salt. Typical case of deposition of ettringite at the macro voids of steel-concrete interface is shown in **Fig. A11**.

3.14 Healing of Voids

After splitting the specimens, white deposit surrounding the visible voids was generally found by naked eye, especially for OPC. Typical SEM micrographs at the void region are shown in **Fig. A12**. It is found that for OPC, significant amount of ettringite is formed at the void region. In the case of SCB, ettringite was observed mostly in the outer region and also in less extent compared to the OPC.

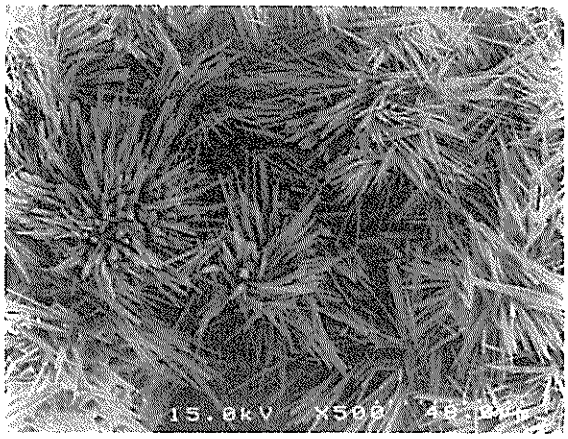

Fig. 38 SEM Micrograph On a Split Open Crack Plane

3.15 Healing of Cracks

Small crack widths ($\leqq$0.5 mm) were healed by autogeneous healing irrespective of the types of cement (Series 2) after 15 years of exposure. **Figure 36** shows a case of crack healing. White deposit was observed at the crack plane. Deposit was also extended on the surface of concrete.

A detail study on the process of autogenous healing in the laboratory concluded that the precipitation of calcium carbonate crystals ($CaCO_3$) in the cracks was almost the sole cause for the autogenous healing of the cracks. The water insoluble $CaCO_3$ is evolved from a reaction between the calcium ions derived from the concrete and the in-water available bicarbonates or carbonates as shown below (**20**):

$$Ca^{++} + CO_3^{--} \Leftrightarrow CaCO_3 \quad (\text{pH of water} > 8)$$

$$Ca^{++} + HCO_3^{-} \Leftrightarrow CaCO_3 + H^{+} \quad (7.5 < \text{pH of water} < 8)$$

The pH of seawater was around 7.8. Presence of alkalis in the crack regions leached from concrete and also alkali deposits produced from the reaction of sea salts and hydrated cement pastes will increase the pH in the crack further. Therefore, the above-mentioned reactions are anticipated for the specimens investigated here.

SEM micrographs across the cracked region are shown in **Fig. 37.** The needle-shaped ettringite was mixed with other deposits, which were confirmed as

$CaCO_3$ and $Mg(OH)_2$ by further investigation. SEM micrograph taken onto a split open healed crack is shown in **Fig. 38**. Clear deposit of ettringite crystals is observed onto the split open crack planes. Results of EPMA mapping for Cl, MgO, and SO3 near the crack region is shown in **Fig. 39**. Cl, CaO, and MgO rich regions are observed near the crack. The corrosion of steel bars at the healed and unhealed cracks is shown in **Fig. 40**. Clear white deposit over the debonded area of the steel bars at the root of the crack is found. It controls the rate of corrosion over the steel bars at the root of the crack. Contrary, steel bars at the root of the unhealed cracks show severe loss of bar diameter. It clearly indicates that for sustainable development of concrete structures under marine environment, the occurrence of crack healing is very essential.

The progress of healing with the variation of the cement types could not be judged from this investigation. However, based on a detail laboratory study, it was concluded that the type of cements has no influence on the autogenous healing (**20**). Therefore, for the same crack widths, the progress of healing can be assumed to be the same irrespective of the cement types.

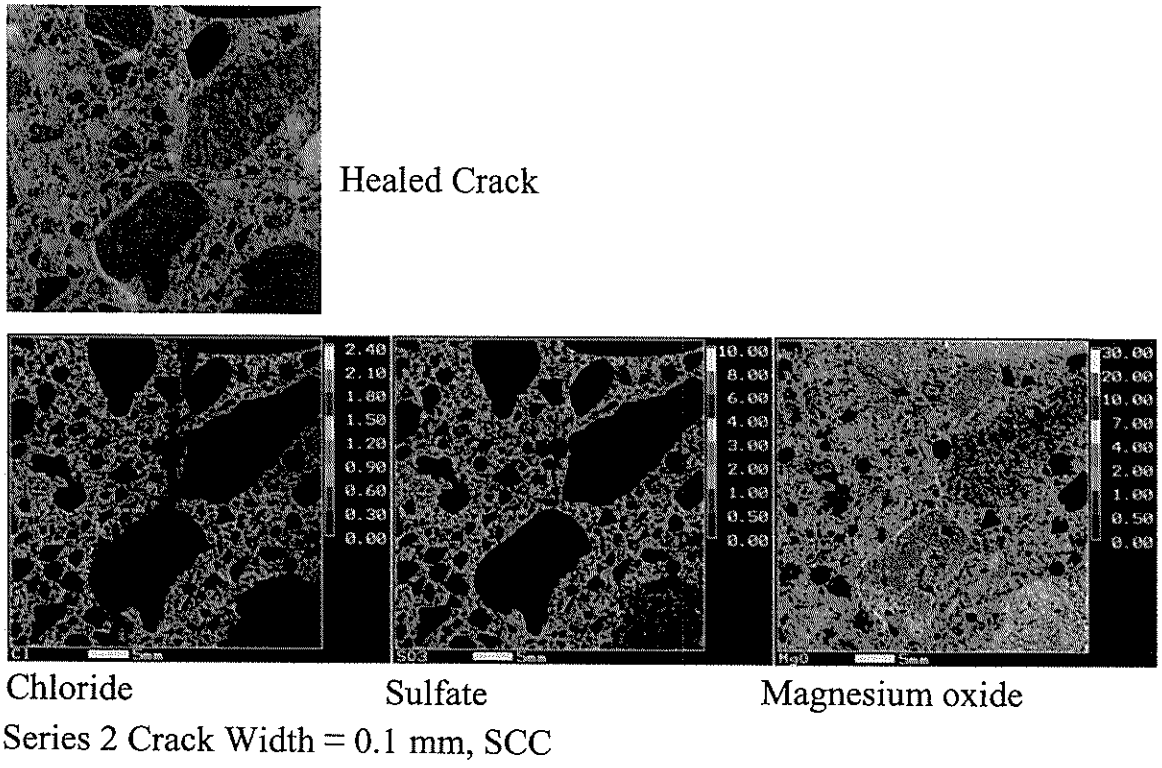

Fig. 39 Richness of Chloride, Sulfate, and Magnesium Oxide Near the Healed Crack

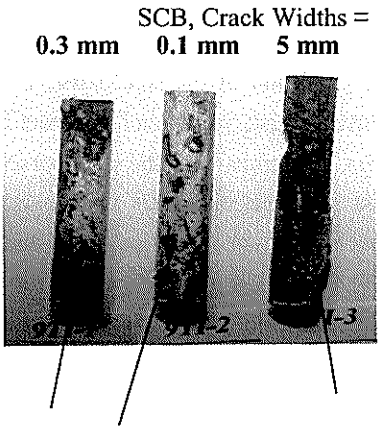

Fig. 40 Corrosion at the Root of Healed and Unhealed Cracks

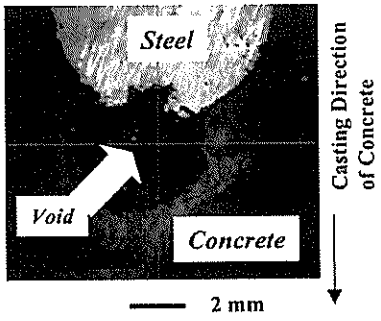

Fig. 41 Corrosion Pits due to the Voids at the Steel-Concrete Interface

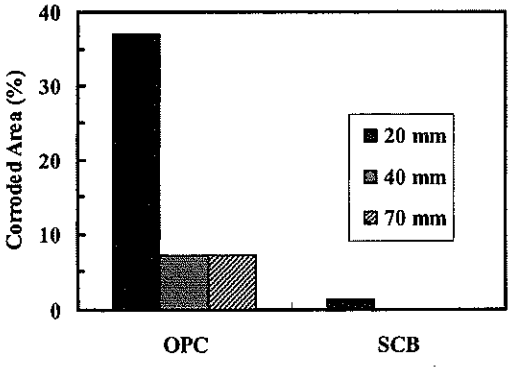

Fig. 42 Corroded Area over the Steel Bars (Series 3)

Table 22 Corroded area of steel bars for the different cover depths – Cylindrical specimens

Cover (cm)	Corroded Area (cm^2)*			
	OPC	SCA	SCB	SCC
2	11.82	10.35	0.51	0
4	1.37	0	0	0
7	0	0	0	0

*Total area of bar = 51 cm^2.

Table 23 Number of pits and maximum pit depth – Cylindrical specimens *

Cover (cm)	Number of Pits and Maximum Pit Depth (mm)				
	OPC	SCA	SCB	SCC	FACB
2	6 (1.5)	3 (1)	0 (0)	0 (0)	5 (0.5)
4	2 (1)	0 (0)	0 (0)	0 (0)	0 (0)
7	0 (0)	0 (0)	0 (0)	0 (0)	0 (0)

* Pit depths <0.5 mm are neglected. The figures in brackets represent the maximum pit depth in mm.

Table 24 Crack widths and maximum pit depths – Prism specimens

Specimen	Crack Width (mm) and Maximum Pit Depths in Cracked and Uncracked Regions (mm) *		
	1	2	3
OPC	0.2 (0.5) ((1.0))	0.1 (0) ((0.5))	0.1 (0.5) ((1.5))
SCA	0.1 (0) ((0))	0.3 (0.5) ((1.0))	0.2 (0) ((0))
SCB	0.3 (0.5) ((0))	0.1 (0) ((0))	***5*** ***(3.5**)*** ***((0))***
SCC	***1.5*** ***(1**)*** ***((0))***	0.1 (0) ((0))	***2*** ***(0.5**)*** ***((0))***

*The figures in (.) and ((.)) represent maximum pit depths in cracked and uncracked regions, respectively. Pit depths < 0.5 mm are not counted. The figures without bracket represent crack widths. Unhealed cracks are shown in bold-italic type.
**Significant loss of diameter observed due to corrosion around the circumference of steel bars.

Table 25 Crack Widths and Total Number of Pits – Prism Specimens

Specimen	Crack Widths (mm) and Pit Numbers		
	1	2	3
OPC	(0.2) 7	(0.1) 5	(0.1) 8
SCA	(0.1) 0	(0.3) 7	(0.2) 7
SCB	(0.3) 2	(0.1) 0	(5) 3
SCC	(1.5) 1	(0.1) 0	(2) 1

The figures in (.) indicate crack widths in mm.

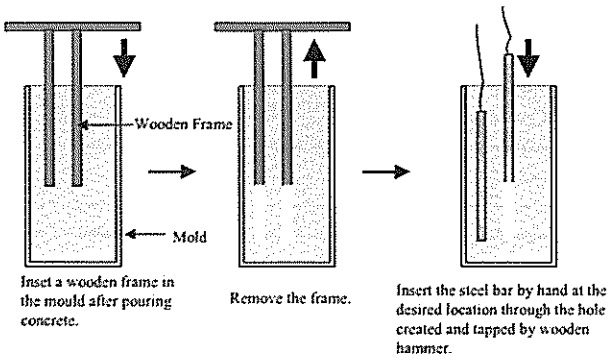

Fig. 43 Special Method of Casting Concrete (Series 1)

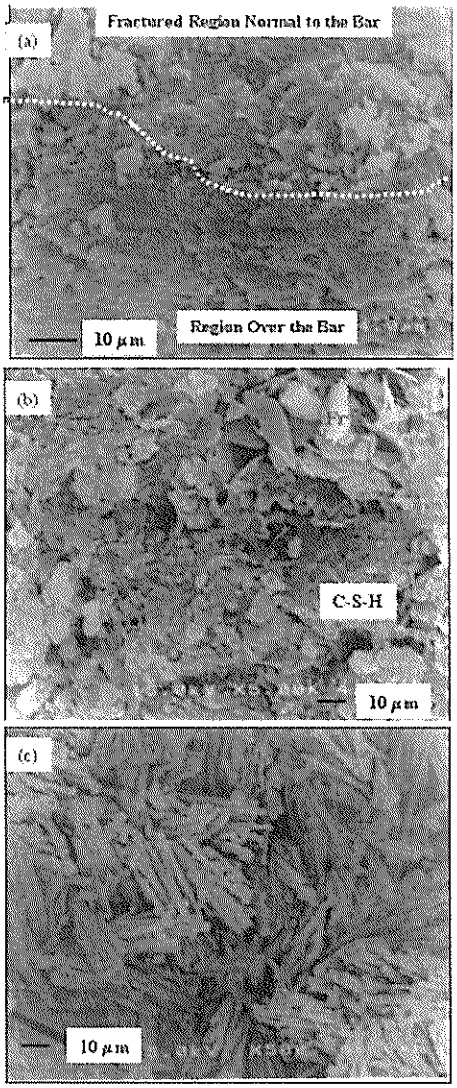

Fig. 44 Top: Steel-Concrete Interface, Middle: Deposit Over the Steel Bars at Voids, Bottom: Voids Over the Steel Bars

3.16 Physical Evaluation of Corrosion

For all series (Series 1~3), the specimens were split opened to see the condition of the steel bars visually, such as the presence of rust, voids over the steel bars. Also, corroded area, pit depths over the steel bars were measured. No rust over the steel bars was found for Series 1, even for chloride concentration more that 2% of cement mass. The same result was observed in tidal and splash exposure zones. It was due to the formation of a good-steel concrete interface due to the special method of casting concrete. This will be discussed later in a separate section.

Corroded area over the steel bars for Series 2 is summarized in **Table 22**. The corroded area was relatively lower over the steel bars embedded in concrete made with slag cements with a high amount of slag, such as 60-70%. The corroded area was also limited to the void region over the steel bars. Corrosion pits were also observed at these locations. A typical case is shown in **Fig. 41**. The authors carried out several detailed investigation to clarify the influence of voids at the steel-concrete interface. Generally, the presence of voids at the steel-concrete interface creates an anodic area even for a very low level of chloride concentrations. These results can be obtained in **References 21 and 22.**

Corroded area over the steel bars after 30 years of exposure is shown in **Fig. 42**. Less amount of corrosion is observed over the steel bars for slag cement (SCB). Same as before, it was also recognized that the voids at the steel-concrete interface leads to the corrosion over the steel bars and later formed pits over the steel bars.

Number of pits and maximum pit depths are listed in **Table 23** for Series 2. Steel bars in concrete made with OPC show more number of pits compared to SCA, SCB and SCC. SCC shows the least number of pits.

The maximum pit depths of the steel bars at the cracked and uncracked regions of prism specimens are listed in **Table 24**. For small crack widths (≦0.5 mm), maximum pit depth is not necessarily observed at the cracked regions. It is explained due to the crack healing. SCC shows the least number of pits. The total numbers of pit are listed in **Table 25**. Pit numbers in the case of slag cements is the least, especially for SCC. For small crack widths (≦0.5 mm), the degree of corrosion of

steel bars is sequenced as OPC>SCA>SCB>SCC as in uncracked concrete. This also confirms the electrochemical results explained before.

For large crack widths (1.5, 2 and 5 mm), significant loss of diameter was observed due to the corrosion of steel bar around the perimeter. Unfortunately, due to the limited number of data relevant to the large crack widths, the performance of the cements investigated here could not be compared. Further investigations are still necessary on this matter. Deep localized corrosion is suspected for slag cements based on the limited numbers of data. It was understood that in order to enhance durability of concrete structures in the marine environment, crack widths should be narrower to allow possible healing during its exposure.

3.17 Improvement of the Steel-Concrete Interface due to a Special Method of Casting Concrete

To avoid the influence of the spacers at the bottom of the specimens, a special method was adopted to place the steel bars in concrete. The method is briefly explained in **Fig. 43**. The insertion of the steel bars sometimes after pouring concrete in the mold creates a uniform and compact steel-concrete interface as shown in **Fig. 44**. Voids are found on the split open concrete surface as shown in **Fig. 45**, however the presence of a tiny hydration layer over the steel bars at the voids prevents the corrosion of steel bars even for chloride concentration more than 2% of cement mass. SEM micrograph of the hydration products over the steel bars at the voids is shown in **Fig. 44**.

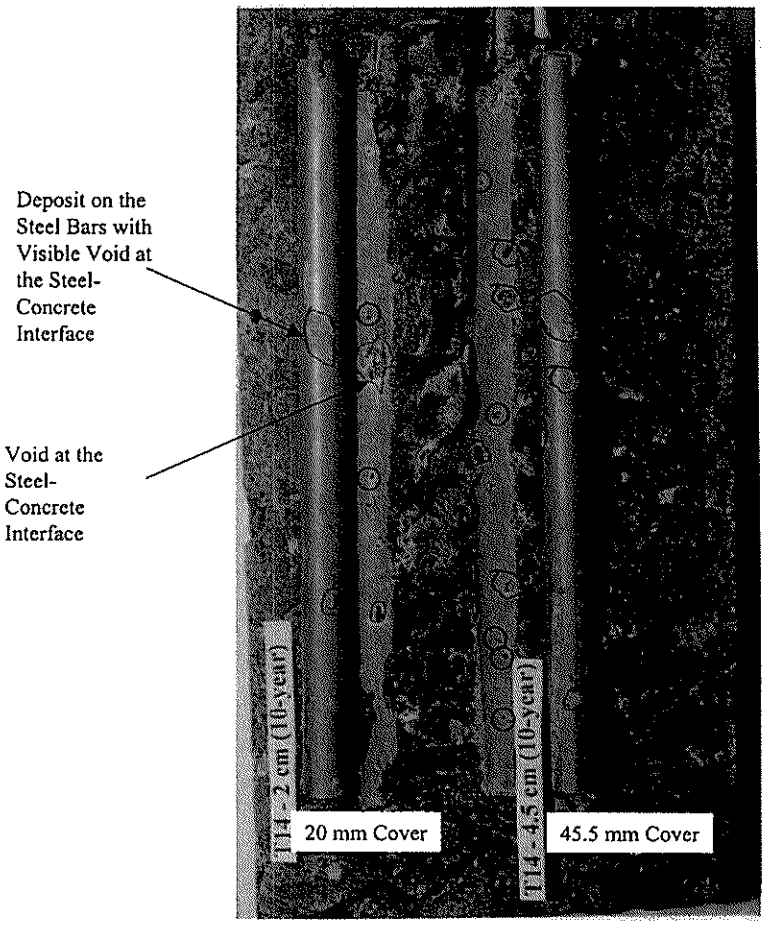

Fig. 45 Split Opened Surface (Series 1)

3.18 Future Investigations

Based on long-term exposure tests explained here, it was clearly understood that slag cement is a best choice for making long-term durable concrete structures under marine environment. However, studies to remove voids from the steel-concrete interface and to make a denser and uniform steel-concrete interface are still necessary to make marine concrete structures for more than 100 years of service life without any major repair works.

4. Conclusions

Based on the investigations on 10 years, 15 years, and 30 years old concrete specimens made with OPC and different slag cements under marine environment, the following major conclusions are drawn:

1. No harmful effect of using slag cements is found after long-term exposure. At the long run, slag cements shows better strength gain compared to the OPC.
2. The outer crust of the specimens made with slag cements becomes denser. It screens chloride and thereby reducing chloride ingress into the inner region. Corrosion of steel bars in concrete is very low for slag cements.
3. Relatively denser interfaces and microstructures are found for slag cements.
4. Voids at the steel-concrete interface initiate corrosion even for a low chloride concentration. Improvement of the steel-concrete interface is necessary to ensure the long-term durability of marine concrete structures.

(Received on February 14, 2003)

Acknowledgement

The authors wish to express their gratitude and sincere appreciation to the authority of *Port and Airport Research Institute, Independent Administrative Institution, Japan* for giving support to perform this study. The authors also thankful to the previous members of the materials divisions for making plan of the specimens before 10 to 30 years.

References

1. Mehta, P. K., Greening of the Concrete Industry for Sustainable Development, ACI Concrete International, Vol. 24, No. 7, July 2002, pp.23-28.
2. Mohammed, T.U., Yamaji, T., and Hamada, H., Microstructures and Interfaces in Concrete after 15 Years of Exposure in the Tidal Environment, *ACI Materials Journal,* Vol. 99, No. 4, July – August 2002, pp. 352-360.
3. Mohammed, T.U., Yamaji, T., and Hamada, H., Chloride Diffusion, Microstructures and Mineralogy of Concrete after 15 Years of Exposure in the Tidal Environment, *ACI Materials Journal*, Vol. 99, No. 3, May – June 2002, pp. 256 – 263.
4. Mohammed, T.U., Fukute, T., Yamaji, T., and Hamada, H., Long-term Durability of Concrete Made with Different Water Reducing Chemical Admixtures Under Marine Environment, in Book "Concrete for Extreme Condition", Eds. Dhir, K. R., McCarthy, M. J., and Newlands, M. D., Thomas Telford Publishing, UK, 2002, pp. 233-243.
5. Mohammed, T.U. and Hamada, H., Durability of Concrete Made with Different Water Reducing Chemical Admixtures Under Marine Tidal Environment, *ACI Materials Journal* (accepted).
6. Mohammed, T.U., Yamaji, T., Toshiyuki, A., and Hamada, H., Marine Durability of 15-Year Old Concrete Specimens Made With Ordinary Portland, Slag and Fly Ash Cement, *ACI SP 199-30,* Volume 2, 2001, pp. 541-560.
7. Mohammed, T.U., Yamaji, T., Toshiyuki, A., and Hamada, H., Corrosion of Steel Bars in Cracked Concrete Made with Ordinary Portland, Slag and Fly Ash Cements, *ACI SP 199-40*, Volume 2, 2001, pp. 699-718.
8. Fontana, M. G., and Greene, N. D., Corrosion Engineering, Second Edition, McGraw-Hill, 1983.

9. Otsuki, N., Nagataki, S., and Nakashita, K., Evaluation of AgNO3 Solution Spray Method for Measurement of Chloride Penetration into Hardened Cementitious Materials, *ACI Materials Journal*, Vol. 89, No. 6, Nov.-Dec. 1992, pp. 587-592.
10. Nagataki, S., Otsuki, N., Hisada, M., and Miyazato, S. (1996), The Experimental Study on Corrosion Mechanism of Reinforced Concrete at Local Repair Part, *JSCE Proceedings*, No.544, V-32, pp.109-119.
11. Hansen, E. J. and Saouma, V.E., Numerical Simulation of Reinforced Concrete Deterioration – Part I : Chloride Diffusion, ACI Materials Journal, Vol. 96, No. 2, March-April 1999, pp. 173-180.
12. BROWN, R.D., Mechanism of Corrosion of Steel in Concrete in Relation to Design, Inspection and Repair of Offshore and Coastal Structures, Performance of Concrete in Marine Environment, ACI SP 65, 1980, pp.169-204.
13. Mohammed, T.U. and Hamada, H., Yamaji, T., Durability of Concrete Made with Different Water Reducing Chemical Admixtures Under Marine Splash Environment, Seventh CANMET/ACI International Conference on Superplasticizers and Other Chemical Admixtures in Concrete, October 20-24, 2003, Berlin, Germany (submitted).
14. Andrade, C., Alonso, C., On-site Measurement of Corrosion Rate of Reinforcements, Fifth CANMET/ACI International Conference on Durability of Concrete, Barcelona, Spain 2000, Proceedings of a Special Technical Session on "Near-Surface Testing for Strength and Durability of Concrete", Ed. Basheer, P.A.M., 2000, pp.171-183.
15. Mehta, P.K., Concrete in the Marine Environment, Elsevier Applied Science, 1991.
16. Otsuki, N., Hisada, M., Diola, N.B., Mohammed, T.U., Experimental Study on Interfacial Transition Zones in Reinforced Concrete, Journal of Materials, Concrete Structures and Pavements, JSCE, No. 592/V-39, May 1998, pp.155-167.
17. Barnes, B.D., The Contact Zone Between Portland Cement Paste and Glass Aggregate Surface, Cement and Concrete Research, Vol. 8, 1978, pp. 233-44.
18. Barnes, B.D., Diamond, S., and Dolch, W. L., Micromorphology of the Interfacial Zone Around Aggregates in the Portland Cement Mortar", J. Am. Ceram. Soc., Vol. 62, No. 1-2, 1979, pp. 21-4.
19. Rilem Report 11, Interfacial Transition Zones in Concrete, Maso, J.C. (Ed.), E & FN Spon, London, 1996.
20. Edvardsen, C., "Water Permeability and Autogenous Healing of Cracks in Concrete," ACI Materials Journal, Vol. 96, No. 4, July – August 1999, pp. 448-454.
21. Mohammed, T.U., Otsuki, N., and Hisada, M., Corrosion of Steel Bars With Respect to Orientation in Concrete, *ACI Materials Journal*, Vol.96, No.2, March-April 1999, pp.154-159.
22. Mohammed, T.U., Otsuki, N., Hamada, H., and Toru, Y., Chloride-Induced Corrosion of Steel Bars in Concrete with the Presence of Gap at the Steel-concrete Interface, *ACI Materials Journal*, Vol. 99, No. 2, March – April, 2002, pp. 149-156.

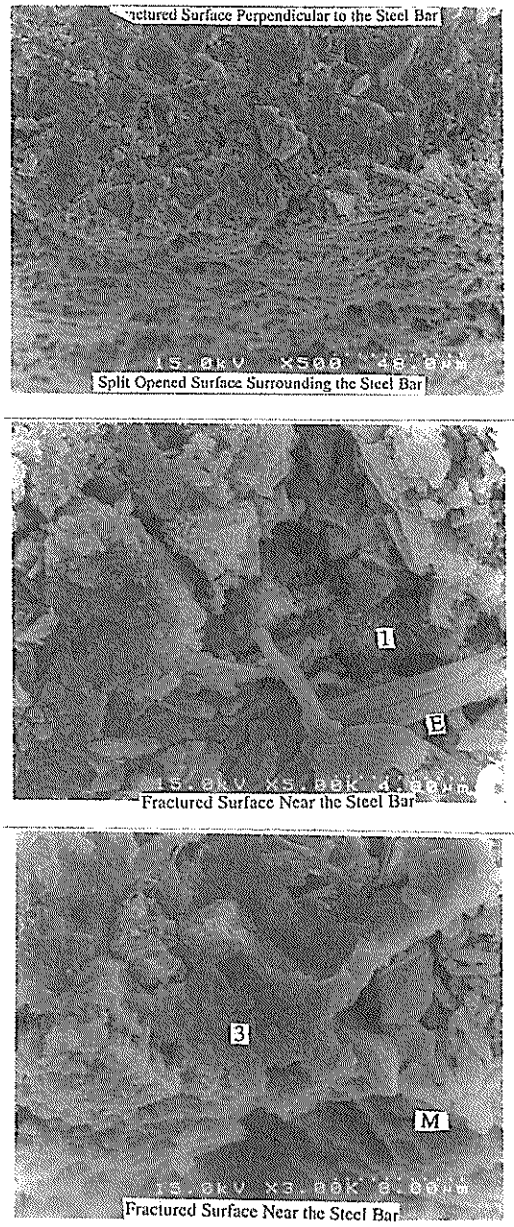

1- Porous C-S-H, 3 – Dense C-S-H, E – Ettringite, M - Monosulfate

Fig. A1 SEM Micrograph of Surface Region Around Steel Bar and Steel Concrete Interface – OPC (Outermost Steel)

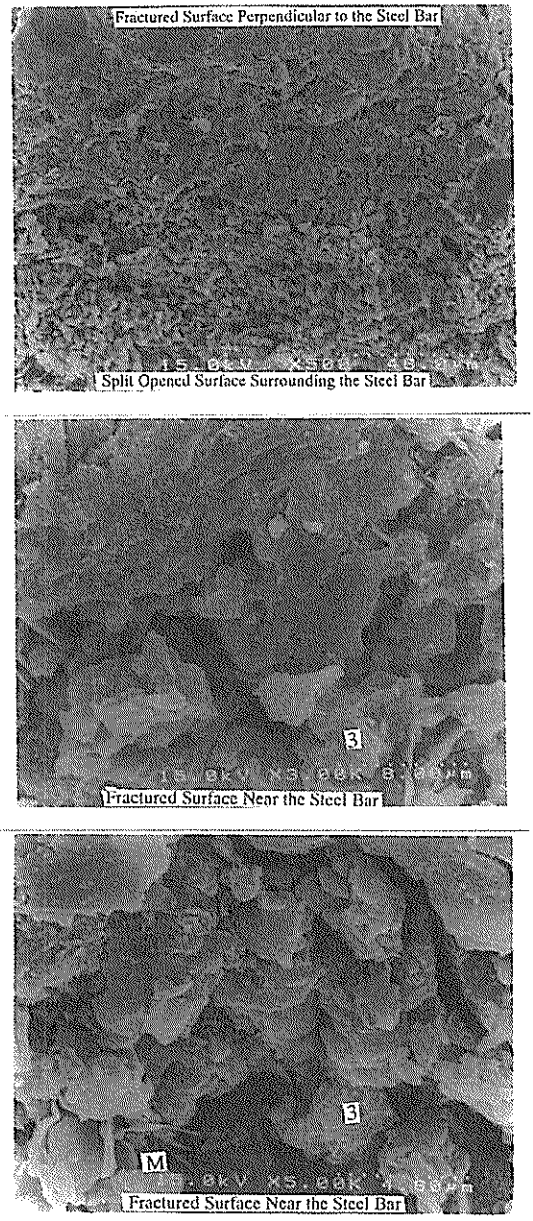

3 – Dense C-S-H, M - Monosulfate

Fig. A2 SEM Micrograph of Surface Region Around Steel Bar and Steel Concrete Interface – SCB (Outermost Steel)

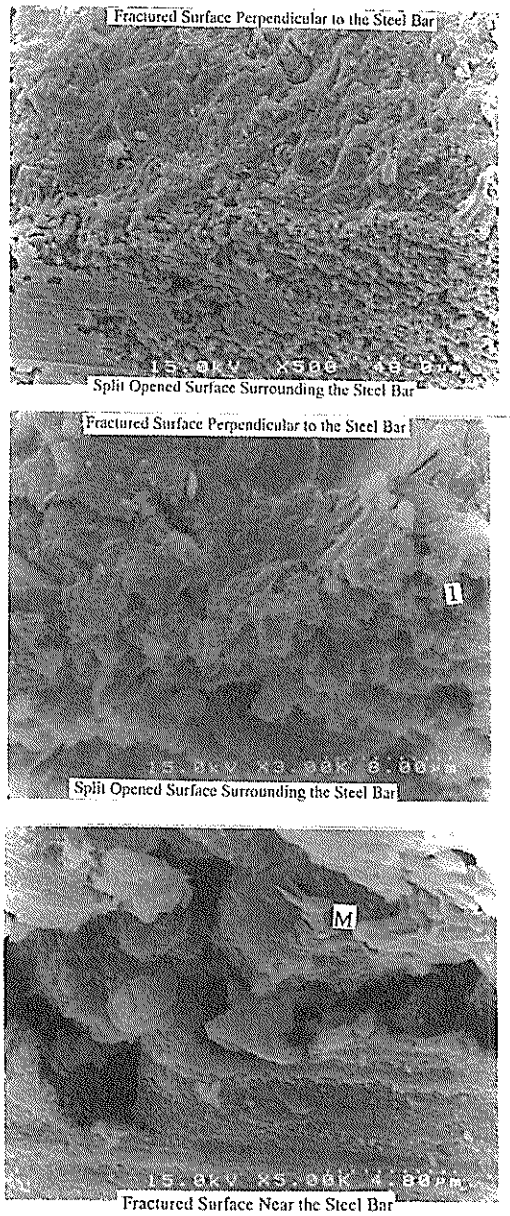

1- Porous C-S-H, M - Monosulfate

Fig. A3 SEM Micrograph of Surface Region Around Steel Bar and Steel Concrete Interface – OPC (Innermost Steel)

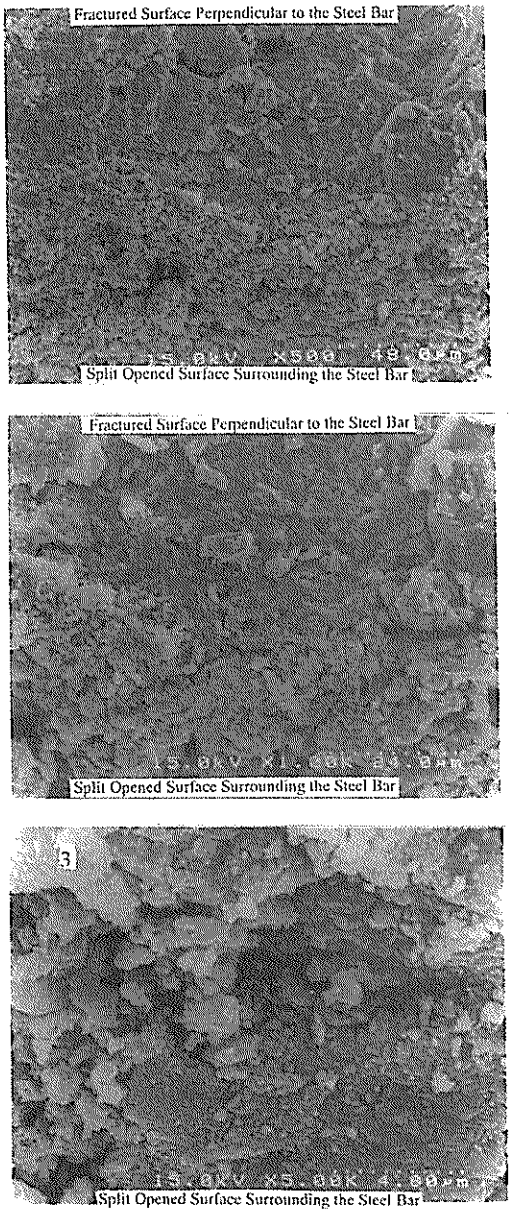

3 – Dense C-S-H

Fig. A4 SEM Micrograph of Surface Region Around Steel Bar and Steel Concrete Interface–SCB (Innermost Steel)

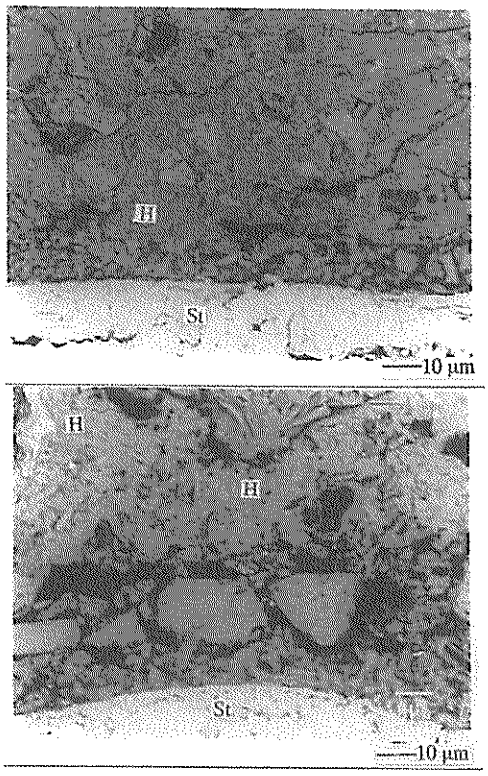

H-C-S-H, St – Steel Bar

Fig. A5 Back-Scattered Electron Image of Steel-Concrete Interface – Innermost Steel (Top- OPC, Bottom – SCB)

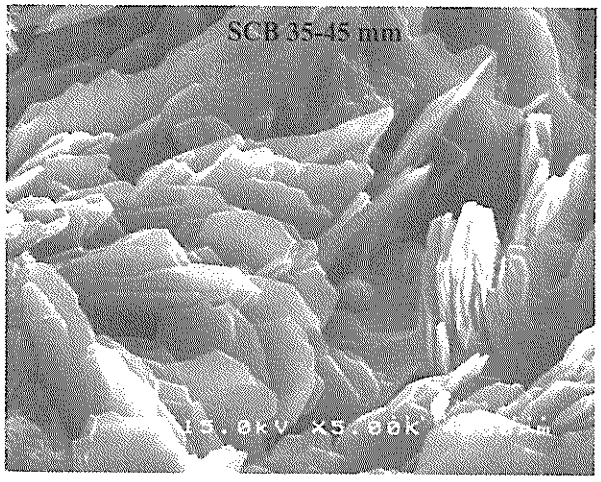

Fig. A7 Typical Friedel's Salt Crystals

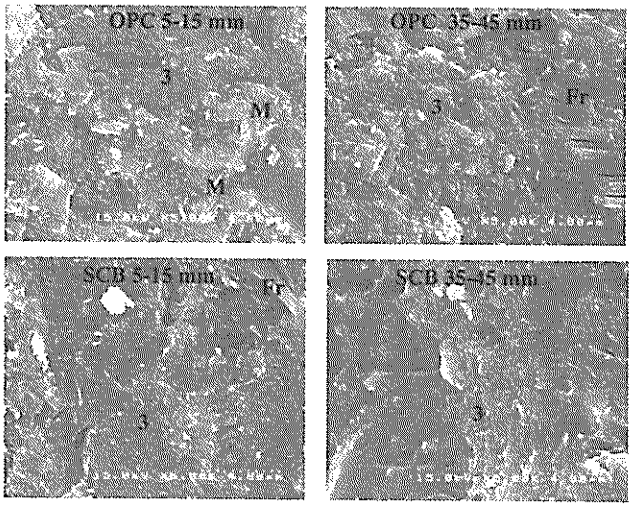

3 – Dense CSH, Fr – Friedel's Salt, P – Ca(OH)2, M – Monosulfate

Fig. A6 SEM Micrographs of the Dense Matrix at the Inner and Outer Regions

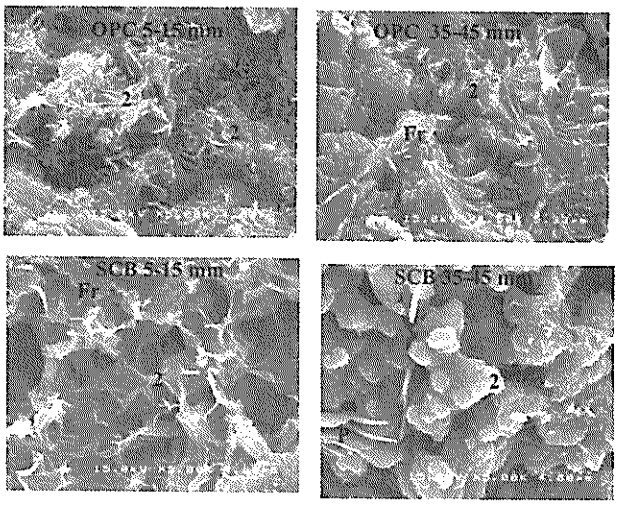

2 – Porous CSH, Fr – Friedel's Salt, P – $Ca(OH)_2$

Fig. A8 SEM Micrographs of the Dense Matrix at the Outer and Inner Regions

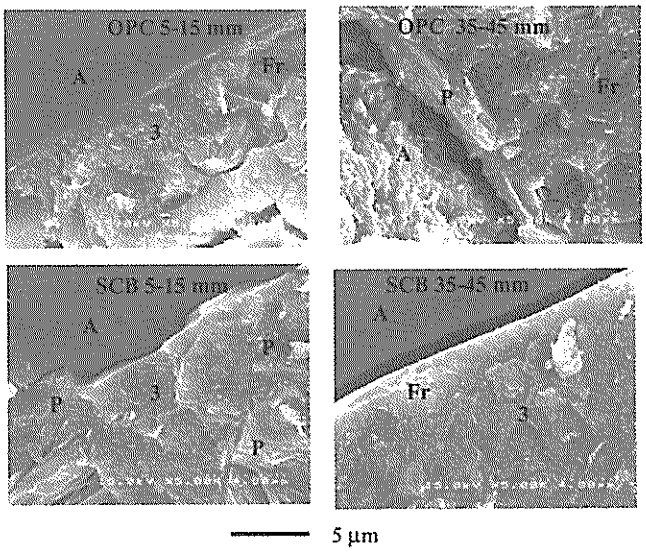

5 μm

3 – Dense CSH, Fr – Friedel's Salt, P – $Ca(OH)_2$
A – Aggregate
Cracks at the interface occur in some cases during sampling.

Fig. A9 SEM Micrographs of the Aggregate-Matrix Interface

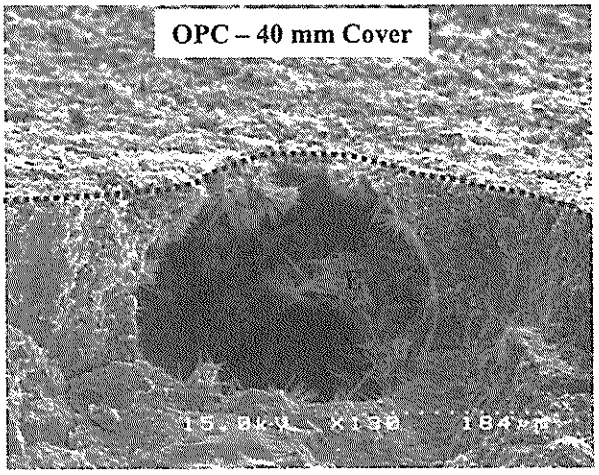

Top – Split Open Surface
Bottom – Fractured Zone

100 μm

E – Ettringite

Fig. A11 Deposition of the Ettringite at the Voids Near the Interface

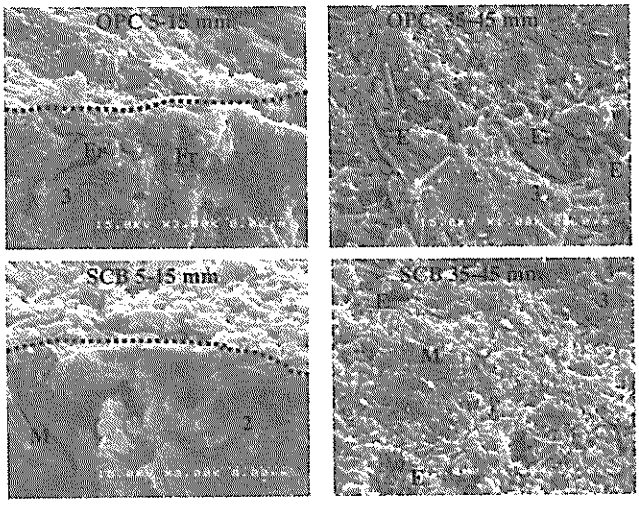

5 μm

10 μm

Over Dotted Line – Split Open Surface
Under Dotted Line – Fractured Zone

Split Open Surface

3 – Dense CSH, 2 – Porous CSH, Fr – Friedel's Salt, P – $Ca(OH)_2$,
M – Monosulfate, E – Ettringite

Fig. A10 SEM Micrograph of the Steel-Matrix Interface

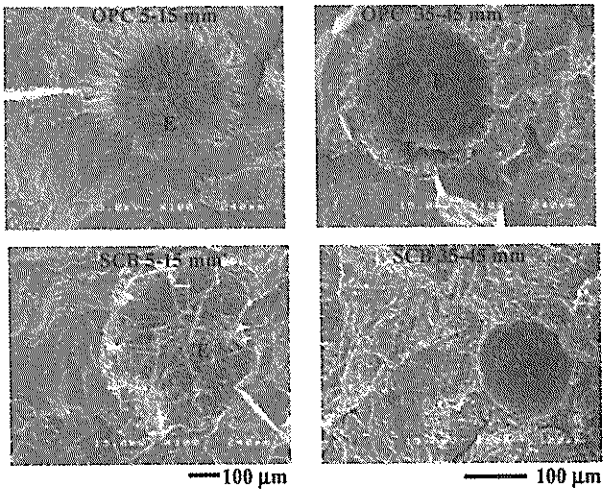

100 μm

100 μm

E – Ettringite

Fig. A12 SEM Micrographs of the Voids